

**Force Feedback for the Patient Side Manipulator
of the daVinci Research Kit**

by

Anna Novoseltseva

A Thesis submitted to the Faculty of the

WORCESTER POLYTECHNIC INSTITUTE

in partial fulfillment of the requirements for the

Degree of Master of Science in Biomedical Engineering

Worcester, Massachusetts

May, 2018

© Anna Novoseltseva 2018

All rights reserved

Approved by:

Prof. Gregory S. Fischer, Advisor
Worcester Polytechnic Institute

Prof. Karen Troy, Committee Member
Worcester Polytechnic Institute

Prof. Loris Fichera, Committee Member
Worcester Polytechnic Institute

Abstract

Teleoperated robotic surgical systems such as daVinci are widely used for laparoscopic surgeries. The currently available daVinci system does not provide haptic feedback. Prior research has shown that the addition of haptic feedback improves surgeons' performance during minimally invasive surgeries. Other authors have implemented haptic feedback in the daVinci robot by placing sensors on the surgical tools, using visual force estimation, and measuring proximal guide wire forces. However, issues with biocompatibility, time delay, low accuracy, and repeatability make them impractical for clinical use. In this work, two strain gauge force-sensing devices were created for the patient side manipulator of the daVinci surgical robot. These devices were designed to be easily added to the existing system. The device mounted on the cannula measures the X-Y components of the forces applied to the tool, and the device mounted on the sterile adapter measures the Z-component of the force. These devices are used for the real-time force feedback in the daVinci robot. The proposed system has high sensitivity and resolution, matches the required force measurement range, and has high signal-to-noise ratio, which implies high signal quality. However,

the absolute errors of the currently built devices are high due to the manufacturing techniques used on the prototype that could be improved upon for a deployed device. This work demonstrates fast 3-DOF force measurements on the daVinci robot without any robot modifications. While the present system has significant systematic errors, these can be mitigated by altering the mechanical design to reduce hysteresis and improve the accuracy of the system.

Contents

Abstract	iii
List of Tables	vi
List of Figures	vii
1 Introduction	1
2 Background	3
2.1 Teleoperated Surgical Robots	3
2.2 Importance of Haptic Feedback	7
2.3 Current Approaches	8
2.3.1 Sensor Placement on Instrument	9
2.3.2 New Instrument Designs	10
2.3.3 Sensorless Methods	11
2.4 Force Sensing Technologies	12
2.5 Contributions	14

3 Force Sensor Design and Characterization	15
3.1 Requirements for the System	15
3.2 Force Measurement	17
3.3 Mechanical Design	18
3.3.1 X-Y Device	18
3.3.2 Z Device	19
3.4 Sensor Placement Optimization	21
3.4.1 Elastic Modulus Measurements	22
3.4.2 Density Measurements	23
3.4.3 Simulation Results	24
3.4.4 Strain Gauge	25
3.4.5 Installation of Strain Gauges	27
3.5 Electrical and Software Design	28
3.5.1 Circuit design	28
3.5.2 Noise Analysis	30
3.5.3 Microcontroller Software	31
3.5.4 ROS Architecture	32
3.6 Calibration	34
3.6.1 Calibration Setup	34
3.6.2 Calibration of the Load Cell	37
3.7 Results	38

3.7.1	Calibration Results	38
3.7.2	Calibration Curve Dependence from Sterile Adapter Position .	43
4	Discussion and Conclusion	47
4.1	Mechanical Design Issues	48
4.2	Electrical Design Issues	51
4.3	Conclusion	51
References		53
5	Appendices	57

List of Tables

3.1	Elasticity Modulus Measurement Data	23
3.2	Material Properties	25
3.3	Sensors Characteristics	43

List of Figures

2.1	The daVinci Xi Surgical System	5
2.2	The Senhance Surgical System	6
2.3	The Senhance Surgical System	8
2.4	Prototype of the 2-DOF Compliant Forceps	9
2.5	Optical Force Sensor	10
2.6	Force-Sensing Surgical Tool	11
2.7	Flowchart of Vision-Based Force Estimation Approach	12
3.1	Developed Force Measuring System Attached to the PSM	17
3.2	Block Diagram	18
3.3	XY-direction Force Feedback Sensor	18
3.4	Displacement of the XY Device	19
3.5	Z-direction Force Feedback Sensor	20
3.6	Z-direction Force Feedback Sensor (Section View)	21
3.7	Setup to Measure Elastic Modulus	22
3.8	Strain in the Device to Measure Forces in X-Y Direction	24
3.9	Strain in the Device to Measure Forces in Z Direction	25
3.10	Block Diagram of the Circuit	28
3.11	Wheatstone Bridge Configuration of the XY-device	29
3.12	Wheatstone Bridge Configuration of the Z-device	29
3.13	Manufactured PCB	30
3.14	FFT Analysis Results	31
3.15	ADC LTC1865 Operating Sequence	32
3.16	ROS Architecture	33
3.17	Block Diagram of the Calibration Setup	35
3.18	Block Diagram of the Load Cell Calibration Setup	37
3.19	Load Cell Calibration Result	38
3.20	Calibration Results of XY Device (n=3)	39
3.21	Calibration Results in Z-direction (n=3)	40
3.22	Sterile Adapter Movement	43
3.23	Sterile Adapter Position Calibration Results for X-direction	45
3.24	Sterile Adapter Position Calibration Results for Y-direction	46

4.1	Actual and Measured Forces in X-direction	48
4.2	Lower Face of the X-Y Device without Tool Shaft	49
4.3	New X-Y Device Design	50
5.1	1st Instrumentation Amplifier	58
5.2	2nd Instrumentation Amplifier	59
5.3	USB-UART Interface	60
5.4	Microcontroller and Power Source	61
5.5	Voltage Converter	62
5.6	PCB Layout	63

Disclaimer: certain materials are included under the fair use exemption of the U.S. Copyright Law and have been prepared according to the fair use guidelines and are restricted from further use.

Acronyms

PSM Patient Side Manipulator

DOF Degrees of Freedom

QTC Pills Quantum Tunneling Composite Pills

RMS Root Mean Square

PCB Printed Circuit Board

ROS Robot Operating System

SD Standard Deviation

SNR Signal-to-noise Ratio

GF Gauge Factor

ADC Analog to Digital Converter

FFT Fast Fourier transform

RMSE Root Mean Square Error

Chapter 1

Introduction

The daVinci surgical system is a robotic platform that enhances surgeons performance in minimally invasive surgeries by enabling highly precise translation of surgeon's hand movements to the instrument's movements.

The currently available daVinci surgery system has a laparoscopic camera, providing visual feedback to guide doctors during surgery. However, the system does not have any kinesthetic or cutaneous feedback, known as haptics [1].

During open surgeries, doctors usually get haptic feedback directly or through the surgical tools. In minimally invasive surgeries interaction with patients via long shafts leads to the loss of some force and tactile sense. In robotic surgery systems, surgeons have to manipulate robots indirectly, which eliminates all haptic feedback [2].

It is believed that the addition of haptic feedback in the daVinci surgery robot will help to reduce the amount of surgical errors and intra-operative injuries, which will

lead to faster post-surgery recovery time and decreased rate of unsuccessful surgeries [2–4].

There are many technical challenges to overcome in order to implement the haptic feedback in the daVinci robot. One of them is getting accurate force readings from the patient side manipulator (PSM). To address this issue, we are trying to create force-sensing device, that can be easily added to the existing surgery system.

Chapter 2

Background

2.1 Teleoperated Surgical Robots

Recently robots have started to be extensively used for surgical procedures. It allows doctors to perform these procedures with high accuracy, repeatability, and reliability, which in turn results in reducing operation time, errors and post-operation injuries. Minimally invasive surgeries are beneficial for accurate procedures with minimal access to operated organs, e.g. neurosurgery, eye surgery, cardiac surgery, intravascular surgeries and etc. Use of robots in minimally invasive procedures improves precision and reliability of operations [5].

There are two types of devices used for surgeries, supporting and augmenting. Supporting devices perform secondary functions to support the surgeon. Some of them used for positioning and stabilization purposes of cameras, endoscopic tools, ul-

trasound probes and etc. Others to increase device dexterity or autonomy (dexterous and autonomous endoscopes).

Augmenting devices are used to extend surgeon's ability in performing an operation. They can be divided into four categories. Hand-held tools are augmenting instruments that used for hand tremors reduction, for dexterity and navigation capability increase. Another type of augmenting devices is cooperatively-controlled tools, where the surgeon and the robot cooperatively manipulate the surgical device (e.g. ROBODOC system, Steady- Hand robot, LARS, the Neurobot, and the ACROBOT system). Teleoperated robots are a type of augmenting tools, where a surgeon (master) controls the movements of a surgical robot (slave) via a surgeon's console (e.g. the daVinci system, Sensei X, Senhance). And autonomous tools, which can perform some tasks (suturing and knot tying) autonomously [5].

Use of teleoperated robots in surgeries can solve many of the conventional surgery problems in terms of more precise manipulation capability, ergonomics, dexterity, and haptic feedback capability for the surgeon. They enhance dexterity by an increase of instrument degrees of freedom, hand tremor compensation, and movements scaling that allows transformation of the control grips large movements into small motions inside the patient. 3-D view with depth perception gives surgeons ability to directly control a stable visual field with increased magnification and maneuverability. All of these enhances the surgeon's performance. However, robot-assisted surgeries are high cost, need large operational room space, do not have established efficacy, and have

a need for tableside assistants. For these reasons ability of hospitals to use surgical robots is low, making their use for routine surgeries improbable [5].

Today, many surgical robotic systems have been commercially developed and approved by the FDA, such as the daVinci surgical system (Intuitive Surgical, Inc., Sunnyvale, CA) (Figure 2.1), Sensei X robotic catheter system (Hansen Medical Inc., Mountain View, CA), FreeHand v1.2 (FreeHand 2010 Ltd., Cardiff, UK), In-vendoscopy E200 system (Invendo Medical GmbH, Germany), Flex robotic system (Medrobotics Corp., Raynham, MA), Senhance (TransEnterix, Morrisville, NC) (Figure 2.3), Auris robotic endoscopy system (ARES; Auris Surgical Robotics, Silicon Valley, CA, USA), The NeoGuide Endoscopy System (NeoGuide Endoscopy System Inc, Los Gatos, CA) [6,7].

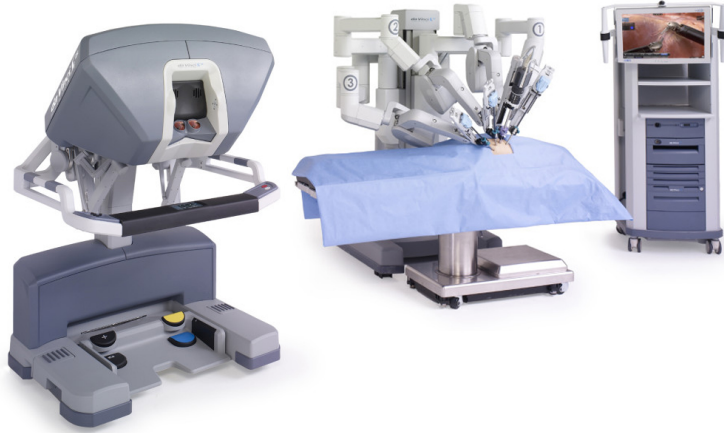


Figure 2.1: The daVinci Xi Surgical System

There is also a number of NON-FDA-approved platforms that currently under development or going through clinical trials. For example, MiroSurge (RMC, DLR, German Aerospace Center, Oberpfaffenhofen-Weling), The ViaCath system (BIOTRONIK,

Berlin, Germany), SPORT surgical system (Titan Medical Inc., Toronto, Ontario), The SurgiBot (TransEnterix, Morrisville, NC), The Versius Robotic System (Cambridge Medical Robotics Ltd., Cambridge, UK), MASTER (Nanyang Technological University and National University Health System), Verb Surgical (Verb Surgical Inc., J & J/Alphabet, Mountain View, CA, USA), Miniature in vivo robot (MIVR) (MIVR, Virtual Incision, CAST, University of Nebraska Medical Center, Omaha, Nebraska, USA), the Einstein surgical robot (Medtronic, Minneapolis, MN) [7].



Figure 2.2: The Senhance Surgical System

The daVinci surgical system is one of the most commonly used robotic surgical systems. In 2015, over 3400 systems were in use around the world. More than 3 million surgeries were performed worldwide using daVinci system [1]. The system has been approved for various types of surgeries such as cardiac, colorectal, thoracic, urological and gynecologic. However, new systems are emerging on the market, providing features that are absent currently in the daVinci System. For example, the

Flex Robotic System, which consists of the flexible endoscope for laparoendoscopic surgeries. This system is able to define a non-linear path to surgical target by advancing a flexible telescopic inner-outer mechanism with instruments inside it, whereas instruments in the daVinci system can follow only non-flexible straight path. Another example is the Senhance robotic platform, which was cleared by the FDA in 2017, that provides actual haptic force feedback, allowing the surgeon to feel forces generated at the instruments end. In addition, the system uses eye-tracking technology to move the camera at the point the surgeon is looking at, while the daVinci uses a footswitch panel to control the camera movement [7].

2.2 Importance of Haptic Feedback

Several studies [8–10] have shown that implementation of force feedback into tele-operated robotic systems can reduce root-mean-square (RMS) and peak values of contact forces, energy consumption, a time required for task completion and the surgical errors rate [5]. The current version of daVinci robot does not provide haptic feedback, an addition of one would be beneficial for both patients and surgeons.

The addition of visual (2.16 1.67), direct (1.62 0.86), or both visual and direct force feedback (2.15 1.08) resulted in lower mean maximum force applied to mitral valve tissue while suturing compared with no force feedback (3.34 1.93 N; P < 0.05). Conclusions To achieve better control of interaction forces on cardiac tissue during

robotics assisted mitral valve annuloplasty suturing, force feedback may be required.

[10]

The experimental results reveal reductions in force error (39.140.9 survey analyses show the effectiveness of the haptic feedback during teleoperation. Conclusions The combined tactile and kinesthetic feedback of the master device in robotic surgery improves the surgeon's ability to control the interaction force applied to the tissue. [8]

As reported by Cundy et al. [7], the experience of each single surgeon may probably explain these results. In fact the personal expertise seems to overcome the lack of a feedback haptic sensor, thus making feedback sensors introduction desirable only if technologically and economically feasible.

Mention

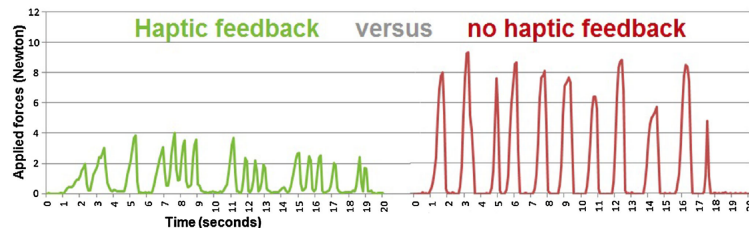


Figure 2.3: The Senhance Surgical System

2.3 Current Approaches

In order to implement haptic feedback in the daVinci system, it is necessary to create force sensing method for surgical tools first. Current approaches of incorporating force sensing include placement of force sensors on surgical tools, change of

instruments design and some sensorless methods.

2.3.1 Sensor Placement on Instrument

Hong et al. suggested measuring pulling and grasping forces at the tip of the surgical instrument by mounting strain gauges on top and bottom surfaces of each of the two flexure hinges of the forceps (Figure 2.4) [11]. RMS errors were close to 0.1 N. One of the disadvantages of this method is biocompatibility issue due to contact of sensors and wires with patient tissues, another is increased cost of each tool. Taking into account that each instrument has limited lifespan [12], it will lead to significant increase in surgery cost.

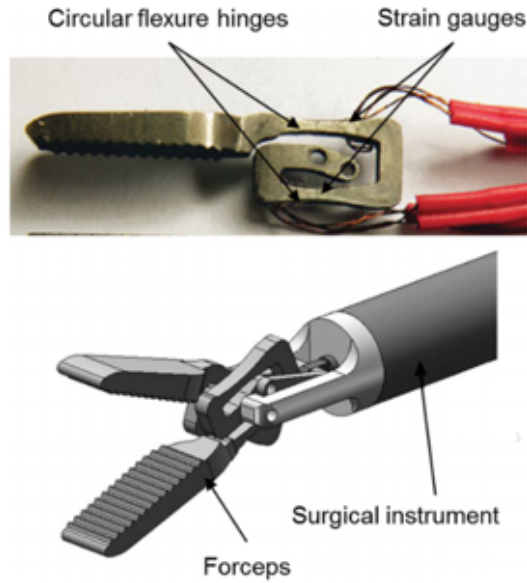


Figure 2.4: Prototype of the 2-DOF Compliant Forceps [11]

Some researchers use optical methods for the force evaluation. These methods

are divided by different sensing principles they use: intensity modulation, wavelength modulation, and phase modulation [13]. Peirs et al. developed 3-axial force sensor that uses light intensity modulation principle [14]. It is based on a flexible titanium structure, that deforms with applied forces (Figure 2.5). These deformations are measured through reflective measurements with three optical fibers. The method shows measurement force range 0.01 N to 2.5 N with 0.01 N resolution. The disadvantage of this method is narrow force measurement range.

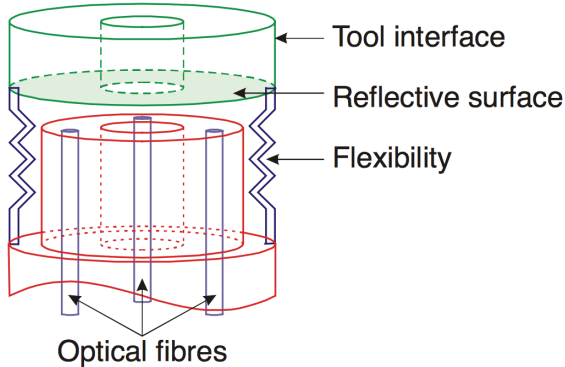


Figure 2.5: Optical Force Sensor [14]

2.3.2 New Instrument Designs

Making new surgical instrument with implemented force sensors is another way to achieve force feedback. Schwalb et al. developed the new force-sensing surgical tool, that uses a proximally located force/torque sensor (Figure 2.6) [15]. This allows avoiding miniaturization and sterilization issues. The method has high sensing accuracy with errors less than 0.09 N. The outer diameter of the developed tool is 12 mm.

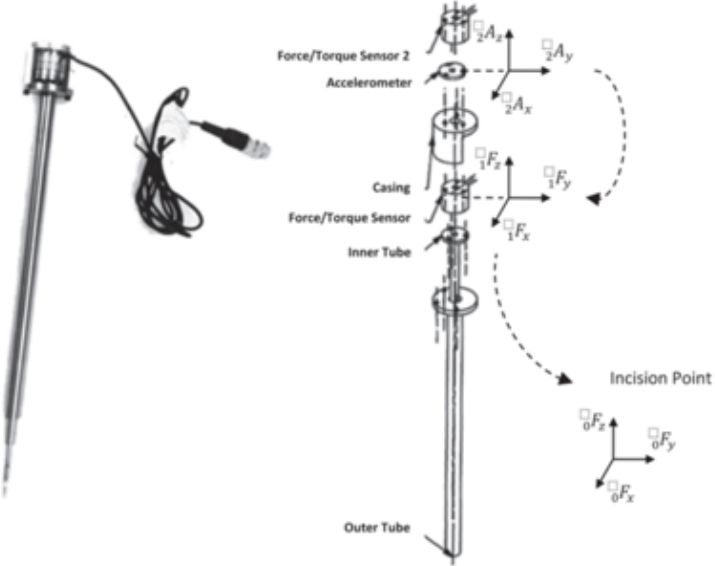


Figure 2.6: Force-Sensing Surgical Tool [15]

This method as well requires an increase in the tool cost, leading to higher surgery expenses.

2.3.3 Sensorless Methods

All sensorless estimation methods avoid drawbacks associated with biocompatibility and integration issues. There are 2 methods: vision-based force feedback and motor currents measurement method.

Aviles et al. proposed to use vision-based solution with supervised learning to estimate the applied forces [16]. After extraction of the motion geometry of the object surface, they use a deep network to learn the relationship between the extracted visual information and the applied force (Figure 2.7). The evaluated average root-mean-square error of the method is 0.02 N. The disadvantage of this methods is

the necessity to know objects material properties, and some materials such as bones would not visually deform. Additionally, the method has significant time delays due to computation time and is not suitable for real-time force feedback.

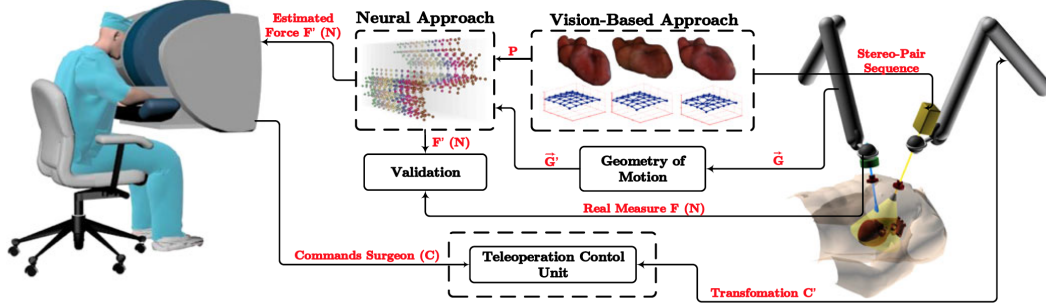


Figure 2.7: Flowchart of Vision-Based Force Estimation Approach [16]

In [17, 18], authors estimate external forces using dynamics models and motor currents from the robot. They linearly parameterized PSM dynamics model and used it to derive forces values. As a result, they implemented sensorless force estimation method and they concluded that it was feasible. Even though, the proposed method does not show sufficient repeatability and accuracy.

2.4 Force Sensing Technologies

For the force sensing depending on their operating principle following types of sensors can be used: piezoelectric, strain-gauges, quantum tunneling composite pills (QTC Pills) or optical sensors [19].

- Piezoelectric sensors consist of two crystal disks with an electrode foil in between. When force is applied, an electric charge, proportional to the applied

force, is obtained and can be measured. Piezoelectric sensors show small deformation when force is applied, this results in a high resonance frequency. Also, piezoelectric sensors due to their principle of operation have significant linearity error and drift [20].

- QTC Pills are flexible polymers, that have exceptional electrical properties. They are made of a nonconducting material that contains small nickel particles. In the resting state, it acts as an insulator, because metal particles are too far from each other. When it is compressed, its conductivity increases and current can pass through it [21]. QTC Pills are very sensitive and can work in wide ranged forces. However, they have an exponential relationship between force and resistance, they are temperature sensitive and depend on charge application time. Meaning they have low accuracy and not suitable for dynamic force measurements [22].
- In the strain gauge based force transducers, the force causes deformation and subsequent linear change in resistance. Strain gauges are usually connected to a Wheatstone bridge circuit, where the output voltage is proportional to the applied force. Strain gauge based transducers provide small individual errors (200 ppm), show no drift, and are therefore appropriate for long-term monitoring tasks. However, they are relatively big, temperature dependent, and have a lower resonance frequency in comparison to piezoelectric sensors [19, 20].

- Optical retro-reflective sensors can be used for the force measurements. Emitter and receiver of these sensors are located at the same host. The light from the emitter goes through optical fibers reaches reflector and the reflected light goes back to the receiver. An interruption of the light beam due to bending can initiate a change of the signal output. Optical sensors are rarely used for force sensing applications because measurement range and sensing accuracy of such sensors are limited [13].

On the basis of the above mentioned, piezoelectric sensors are preferable for dynamic measurements of small forces while strain gauge sensors are better when large forces are measured. In this study, strain gauges were used since they show better accuracy and long-term stability [19, 20].

2.5 Contributions

Force sensing devices for measuring forces in X-Y direction and one for Z-direction measurement were created. They allow getting force readings from the daVinci tools of the PSM. These devices can be easily added to the existing daVinci system. Since we have to add created device on each robot arm only, it is cheaper than placement of sensors on each separate surgical tool. Moreover, the created devices allow measuring forces faster than through the visual data processing method and could show better precision than the motor current method.

Chapter 3

Force Sensor Design and Characterization

This chapter sets the requirements for the force sensing system, explains the methodology of the force-sensing devices creation, including mechanical, electrical, and software design, and finally describes the calibration process of the created system and shows the calibration results.

3.1 Requirements for the System

First, from the literature review following requirements for the force sensing device were outlined:

- ***Biocompatibility.*** Z-device is attached to the sterile adapter and does not

have to be biocompatible. However, the X-Y device goes inside the patient, it means that it should be sterilized and biocompatible.

- **Force range.** Some studies [23,24] have shown that force range applied during surgeries lies in range ($0 - 11N$). The designed device need to measure forces in that range, and if the force goes beyond that range it can be used to trigger safety alert.
- **Force sensitivity.** The device should be sensitive enough with resolution at least $0.05N$ and give accurate readings ($error < 0.1N$) [23].
- **Speed of force reading.** The device is used for real-time haptic feedback, the minimum requirement for data acquisition speed is 1 kHz [25].
- **No restriction of motion range of the device.** The forces should be measured in three directions independently from each other. At the same time tool should freely rotate and change the depth of insertion.
- **Linearity.** Calibration curve of created sensors should be linear.
- **Device modularity.** Force-sensing devices should be designed so they can be easily added to the existing system and fit daVinci cannula and sterile adapter.

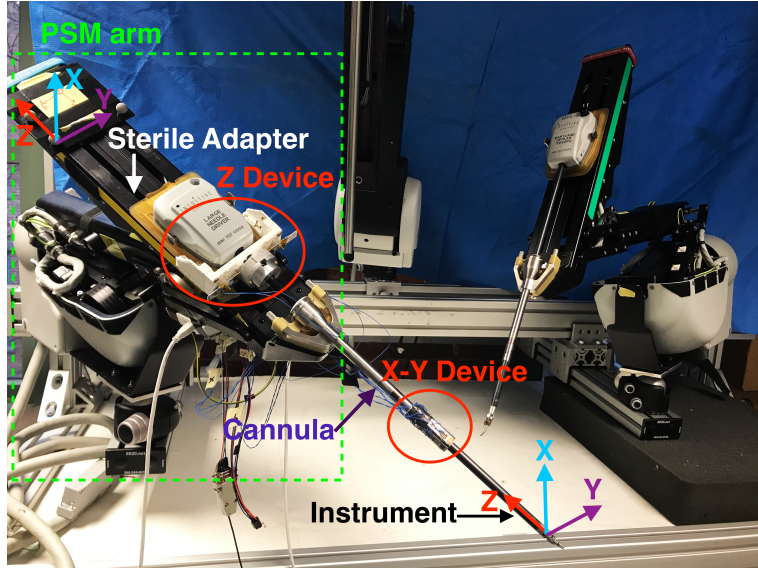


Figure 3.1: Developed Force Measuring System Attached to the PSM. The daVinci instrument is inserted in the sterile adapter of the PSM arm. Z Device is attached to the sterile adapter. XY Device is press-fitted on the cannula end.

3.2 Force Measurement

A block diagram of the created system for 3-DOF force measurement is shown in Figure 3.2. Forces that applied on the end of the surgical tool are measured using strain gauges, which change their resistance with force. Using created printed circuit boards (PCBs), these resistance changes are measured and published within ROS. At the same time, we measure a current joint position of the tool, which is needed for the force calibration. The position data and data from PCBs are used to find values of the force in X, Y, Z directions (Figure 3.1).

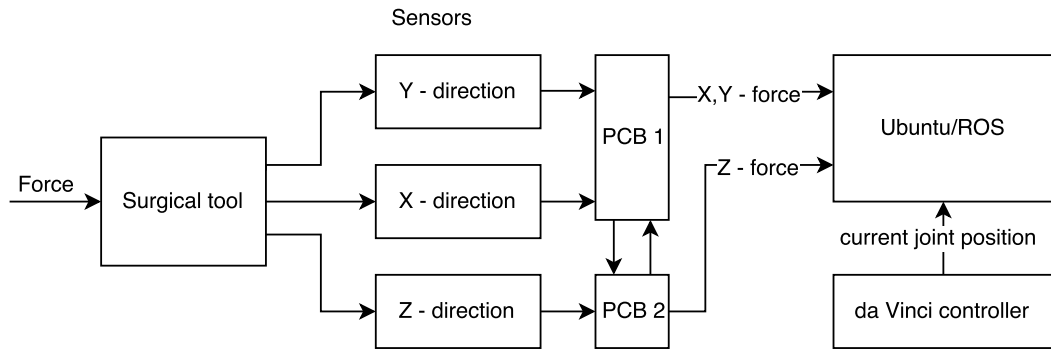
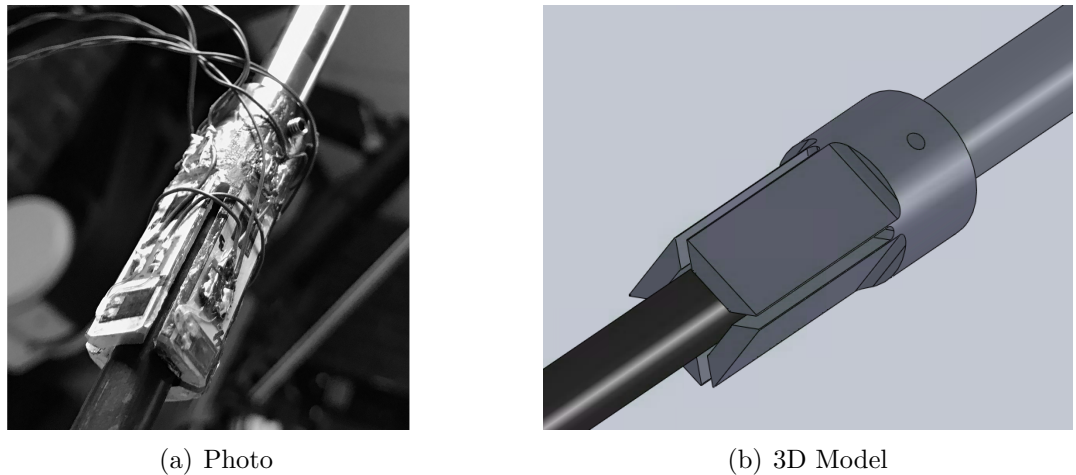


Figure 3.2: Block Diagram

3.3 Mechanical Design

This chapter describes mechanical design of two sensors, one for measurement X-Y component of the force, another for Z-component of the force.

3.3.1 X-Y Device



(a) Photo (b) 3D Model

Figure 3.3: XY-direction Force Feedback Sensor

The XY-device consists of one sleeve and one set screw. We manufactured sleeve

using Aluminum 6061 Alloy. The manufactured sleeve is placed on the cannula end and is fixed with a set screw on the top (Figure 3.3). The sleeve was manufactured slightly wider than the cannula to compensate tolerances in cannula sizes.

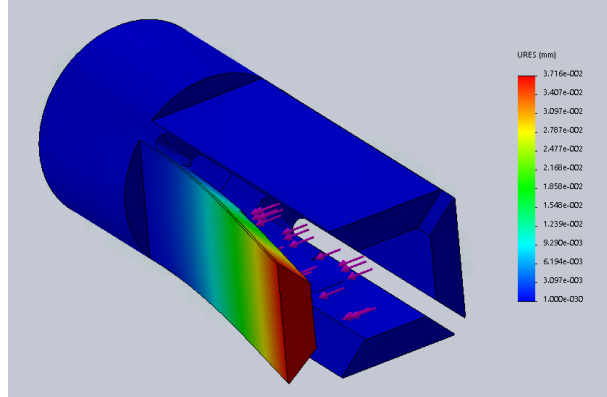
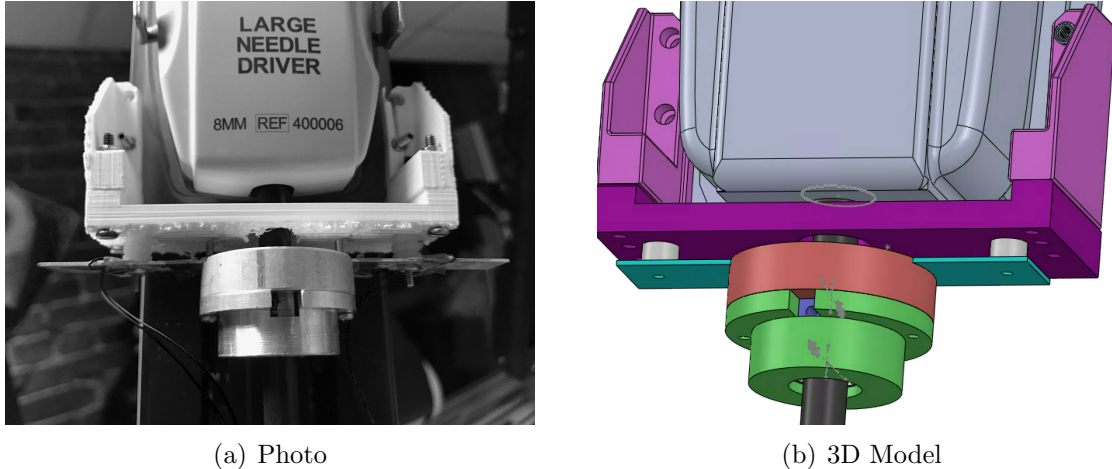


Figure 3.4: Displacement of the XY Device

In order to get accurate readings maximum displacement of the sleeve sides should prevent shaft from hitting the cannula. It means that it should be less than distance between the cannula and the instrument shaft $d = (d_{can} - d_{shaft})/2 = (8.75 - 8.4)/2 = 0.175$ mm, where d_{can} is inner diameter of the cannula and d_{shaft} is outer diameter of the shaft. From the Solidworks simulation (Figure 3.4), maximum displacement is 0.037 mm, which is in appropriate range.

3.3.2 Z Device

Z-device principle of work based on the manufacturing imperfections of the connection between the sterile adapter and the surgical instrument, that resulted in movement of the instrument for approximately 0.3 mm.



(a) Photo

(b) 3D Model

Figure 3.5: Z-direction Force Feedback Sensor

Z-device (Figures 3.5 - 3.6) consists of attachment to the sterile adapter, 2 thrust ball bearings, three rings, plate, and two cylindrical spacers. Three rings and two ball bearings are used to transfer only z-directional forces further to the plate and keep the ability of the shaft to rotate. The ring in the center is in direct contact with the instrument shaft, two outer rings are for the push and pull forces transfer. The plate experience maximum strain and all strain gauge sensors are mounted on it. Two cylindrical spacers are used to give plate space to move and they are mounted on the attachment plate. The attachment plate consists of three plates, they are press-fitted on the sterile adapter and fixed with four set screws.

Three rings and plate were manufactured with Aluminum Alloy 6061, attachment parts were 3-D printed, fasteners were used as spacers.

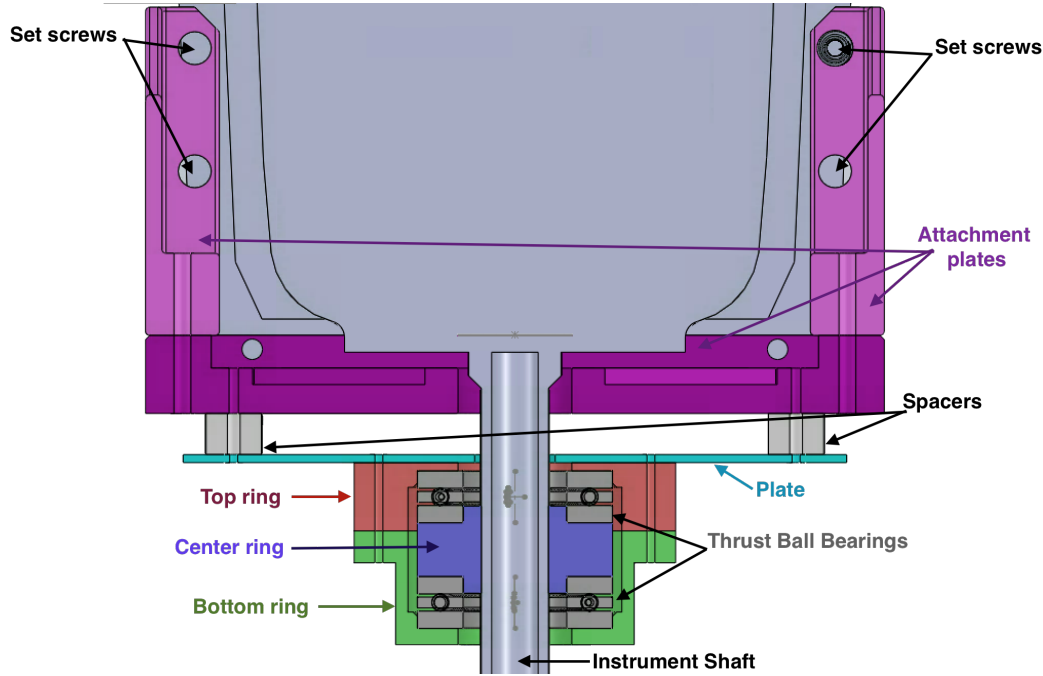


Figure 3.6: Z-direction Force Feedback Sensor (Section View). Center ring in direct contact with instrument shaft, the contact was created using set screw. Thrust ball bearings are used to transfer only Z-component of the force. Top and bottom rings transfer push and pull forces to the plate. Spacers are used to give a space for plate to move. Set screws are used to fit attachment plates on the sterile adapter

3.4 Sensor Placement Optimization

In order to accurately measure forces, the strain gauges should be placed in the area with the highest strain. A finite element analysis was done in Solidworks to find strain distribution and assess the better mounting location of the strain gauges on the created devices. In order to run finite element analysis material properties, such as elastic modulus, Poisson's ratio, and density are necessary to know. Devices material is aluminum 6061, which has elastic modulus 68.9 GPa, Poisson's ratio 0.33, and density 2700 kg/m³ [26]. Since the shaft and cannula materials are unknown, in

order to run finite element analysis their elasticity modulus and density were found experimentally.

3.4.1 Elastic Modulus Measurements

Elastic Modulus of the shaft and the cannula were found experimentally (Figure 3.7). One end of the observing sample (shaft/cannula) was fixed and the force was applied to the other end. We used weights 250g for the shaft and 555g for the cannula to apply forces. The deformation caused by forces was detected with a dial indicator. The experiment was repeated 5 times, average displacement value was used to calculate elastic modulus. Results are shown in Table 3.1.

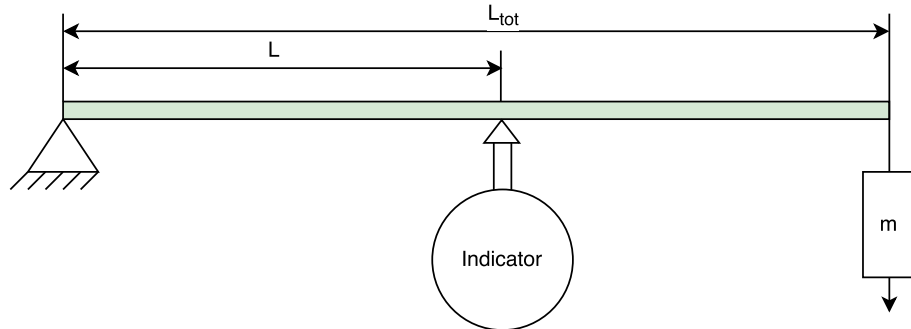


Figure 3.7: Setup to Measure Elastic Modulus

Elastic Modulus was found using the following equation:

$$E = \frac{FL^3}{3\delta I} \quad (3.1)$$

where F - force, L - length from the fixed point to indicator, I - area moment of inertia, δ - displacement.

Area moment of Inertia:

$$I = \frac{\pi(d_o^4 - d_i^4)}{64} \quad (3.2)$$

where d_o - cylinder outside diameter, d_i - cylinder inside diameter.

Force acting on indicator:

$$F = \frac{L_{tot}}{L} mg \quad (3.3)$$

where L_{tot} - total length of the object, m - mass of the weight, g - gravitational constant.

Experimentally found the mean value of elastic modulus of the shaft is equal to 44.31 GPa with standard deviation (SD) 1.86 GPa, an elastic modulus of the cannula is 63.92 GPa with SD 2.97 GPa.

Table 3.1: Elasticity Modulus Measurement Data

Component	d_o , mm	d_i , mm	I , mm^4	m , g	F , N	L , mm	L_{tot} , mm
Shaft	8.4	6	$1.808 \cdot 10^{-10}$	250	3.25	276.2	366.8
Cannula	10.54	8.75	$3.181 \cdot 10^{-10}$	555	6.011	95.5	105.55
Component	$\delta \pm SD$, mm		$E \pm SD$, GPa				
Shaft	2.856 ± 0.123		44.31 ± 1.86				
Cannula	0.086 ± 0.004		63.92 ± 2.97				

3.4.2 Density Measurements

Density was found using following equation:

$$p = \frac{m}{V} \quad (3.4)$$

where m - mass, V - volume.

Weight was measured using mechanical scale. Volume of the shaft was found by following equation: $V = \pi h(r_o^2 - r_i^2) = 4.36 \cdot 10^{-5} m^3$. Volume of the cannula was found using water displacement method. Shaft material density is 473 kg/m^3 , cannula material density is 55238 kg/m^3 .

3.4.3 Simulation Results

The mounting location of the active strain gauges should be under the greatest amount of strain. From the Figure 3.8, it can be seen that strain gauges for X-Y direction device should be mounted on the area shown green, that corresponds to strain value approximately equal to $1.5 \cdot 10^{-4}$. Passive strain gauges, that will be used only for temperature compensation, will be placed in the blue area perpendicular to the active strain gauges.

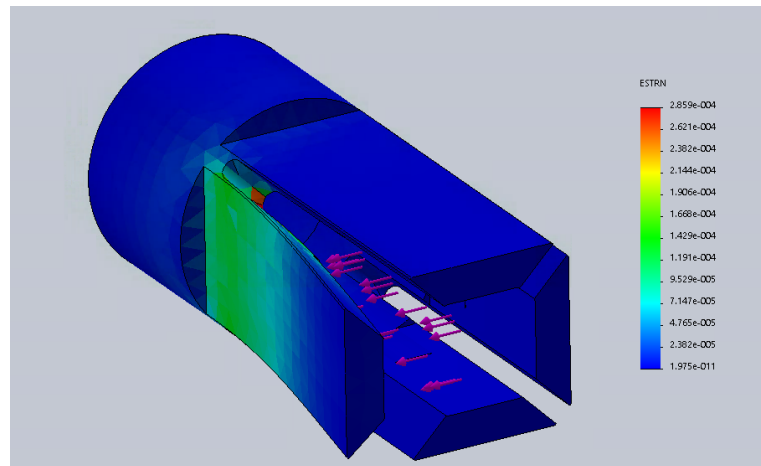


Figure 3.8: Strain in the Device to Measure Forces in X-Y Direction

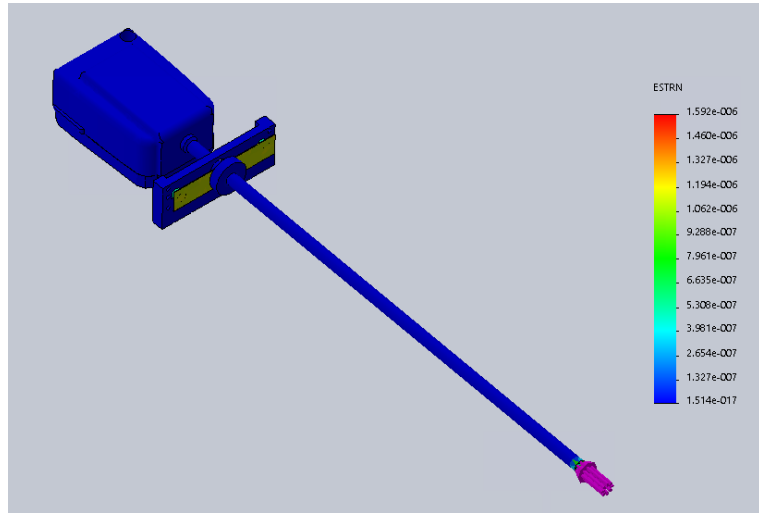


Figure 3.9: Strain in the Device to Measure Forces in Z Direction

Table 3.2: Material Properties

Component	Elastic Modulus, GPa	Density, kg/ m ³
Shaft	44.31	473
Cannula	63.92	55238
Sleeve	68.9	2700

For Z-direction measurement forces (Figure 3.9), the area shown with yellow-green color under the highest strain. On both sides and both ends of this plate strain gauges should be placed to form the full bridge.

All material properties used for simulations are listed in Table 3.2.

3.4.4 Strain Gauge

According to the manual for strain gauge selection provided by Vishay Micro-Measurements, the strain gauge should have following parameters:

- Single grid for unidirectional force measurements;
- Isoelastic (D alloy) that has higher gauge factor with E backing;
- Encapsulated with pre-attached leads for easier placement;
- STC (self-temperature-compensation) - small temperature dependence;

From the FEM analysis, the maximum strain on the created device is $1.5 \cdot 10^{-4}$, in case of 10 N load with the maximally opened shaft. From the literature, strain gauges length should be more than 5% of maximum strain, hence, the minimum length of the strain gauge should be 0.0075 mm.

Gauge Factor (GF) for strain gauges usually is 2. According to the formula (3.5) strain gauge with resistance 120Ω have maximum change in resistance equal to 0.036Ω , and $350 - 0.105 \Omega$:

$$\Delta R = GF \cdot R \cdot \varepsilon \quad (3.5)$$

where GF - gauge factor, R - resistance, ε - strain.

For the device strain gauges with resistance 350Ω , GF is 2, single grid, encapsulated with pre-attached leads were used.

3.4.5 Installation of Strain Gauges

Application of strain gauges was done following the manual provided by Vishay Micro-Measurements [27].

First, the working surface (glass) and tweezers were cleaned with Neutralizer 5. After that shaft surface preparation was started, using solvent degreaser GC-6 Isopropyl Alcohol. A gauge layout was then applied with a 4H drafting pencil. The surface was then conditioned with Conditioner A and the extra liquid was wiped with gauze. Finally, the surface was then neutralized with M-Prep Neutralizer 5A [27].

The strain gauges were first placed on the glass and then transported using mylar tape onto the instrument surface. A thin layer of catalyst was applied to the strain gauge and given one minute to dry. Then adhesive M-BOND 200 was applied on the surface, the pressure was applied on the tape for one minute, then two more minutes to let it dry before the tape was removed. Then leads soldering was done by application of pads, and soldering them with thin wires [28].

The methodology of the strain gauge application more specifically described in [27]. In compliance with the application guide, the same materials and technique can be used to apply strain gauges on different materials (metals, plastics).

3.5 Electrical and Software Design

3.5.1 Circuit design

Signal waveforms and the block diagram of the developed PCB are shown on Figure 3.10.

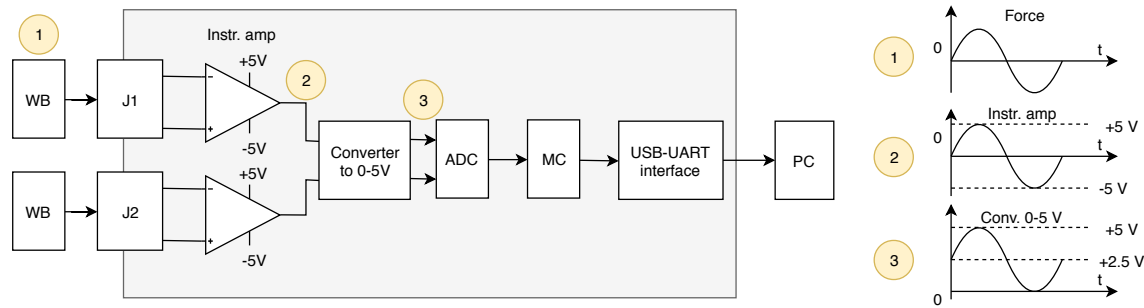


Figure 3.10: Block Diagram of the Circuit

Four strain gauges are connected to form a Wheatstone bridge circuit. On Figures 3.11 - 3.12 placement of strain gauges (1-4) and their Wheatstone bridge configurations are shown for both devices. Strain gauges deform due to applied forces, and it causes the voltage change on Wheatstone bridge. The output signal from the Wheatstone bridge goes to the instrumentation amplifier. Since ADC can convert only positive voltage, voltage converter changes voltage range of the output signal from ($-5V$ to $+5V$) to ($0V$ to $+5V$) range. That signal is converted to the digital signal with 16-bit ADC, which communicates with the microcontroller via SPI interface. The output signal is transferred to the computer via USB.

Using Altium Designer 15.1 the PCB design was developed and manufactured at

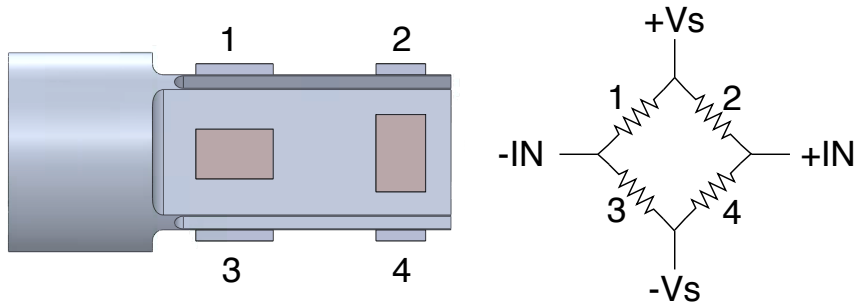


Figure 3.11: Wheatstone Bridge Configuration of the XY-device

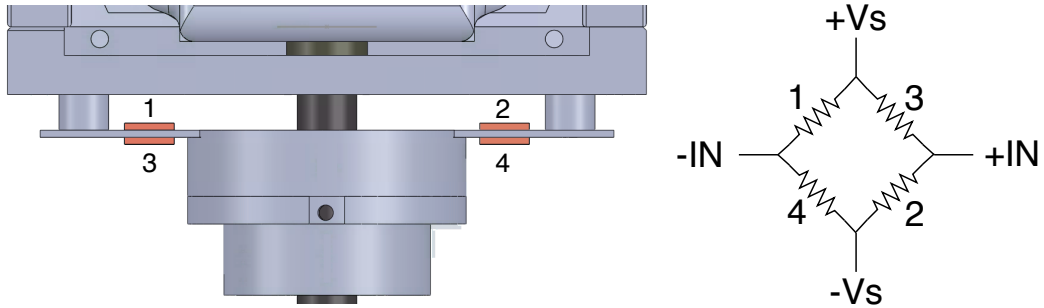


Figure 3.12: Wheatstone Bridge Configuration of the Z-device

Advanced Circuits [29].

In the developed PCB (Figure 3.13) trimpots are used for calibration of the instrumentation amplifier gain (shown yellow) and change of reference voltage (shown red).

Instrumentation amplifier gain change is needed to set up appropriate measuring force range (0-11 N). During calibration, when 11 N applied on the tool end, the output signal (that goes to ADC) should be smaller than 4 V. When the same force applied in the opposite direction, the output signal should be bigger than 1 V.

Reference voltage change is used for the compensation of Wheatstone bridge unbalance caused by strain gauge resistance tolerances. During the calibration, it should

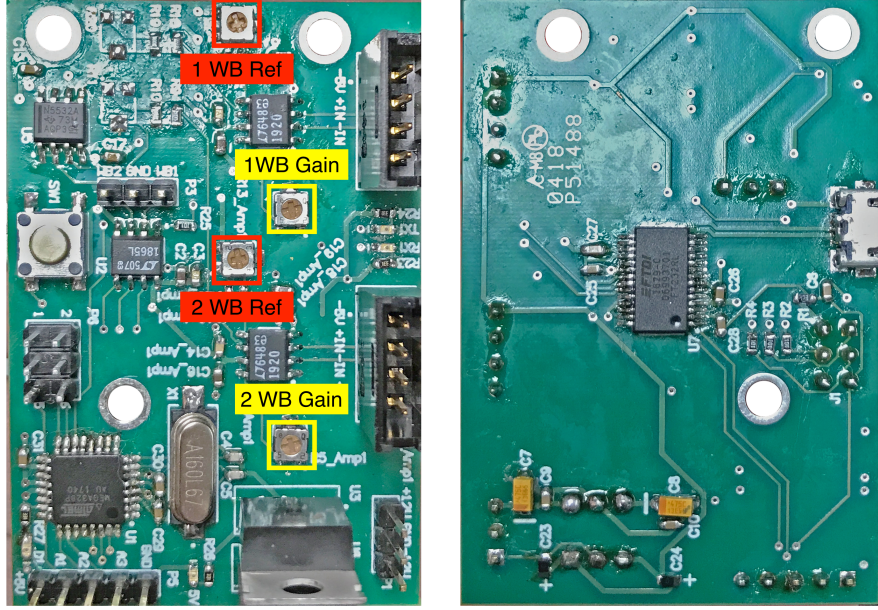


Figure 3.13: Manufactured PCB

be tuned until it gives the output signal close to 2.5 V when no forces applied on the device.

3.5.2 Noise Analysis

Fast Fourier transform (FFT) waveform analysis of the noise signal was performed using Tektronix MSO 4034 Mixed Signal Oscilloscope. The oscilloscope automatically applied the Hanning window, which has good frequency resolution and reduced spectral leakage [30].

The signal frequency from the force sensor should be in the range of (0 to 1 kHz). From the FFT analysis results (Figure 3.14) it can be concluded, that the noise frequency is in range (2.5 kHz and higher) with amplitude (-50 mV to 70 mV)

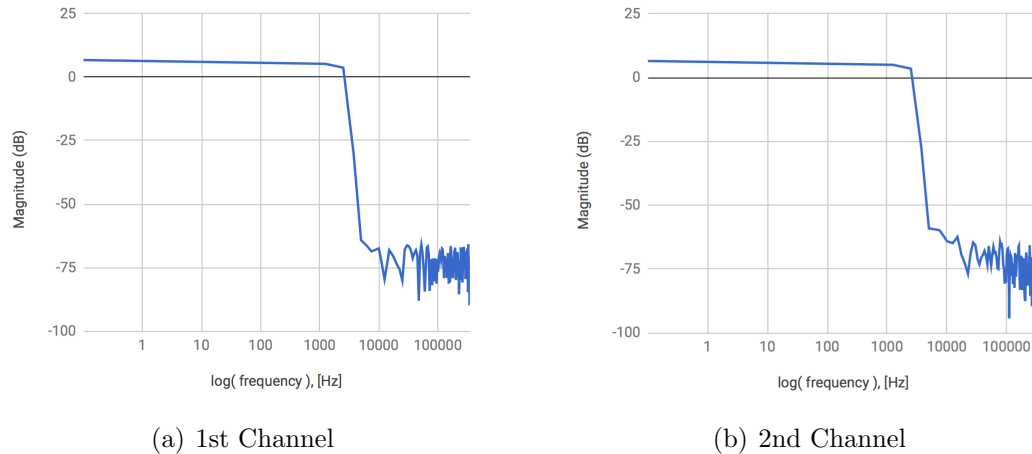


Figure 3.14: FFT Analysis Results

for both channels. That means low pass filter with cutoff frequency 2 kHz should be applied to the output signal. It was decided to use data averaging due to its simplicity of implementation and small time delays. It is an equivalent of low pass filtering that compensates the high-frequency noise [31].

3.5.3 Microcontroller Software

Microcontroller ATMEGA328P is used in the developed PCB for data acquisition, filtering, and sending to ROS. The microcontroller has open-source packages for serial communication with ROS. The microcontroller is programmed to initialize ros nodes with names "adc_xy" for XY-device and "adc_zlc" for Z-device. The master-slave communication is created between X-Y and Z- devices for data acquisition synchronization by sending start conversion signals between two PCBs. When one of the devices gets the signal it starts to communicate with ADC though SPI

interface (Figure 3.15) [32]. The acquired data is filtered from the high-frequency noise by averaging of the 5 most recent readings. And the filtered data is published through the serial port with the baud rate 115200 bits per second.

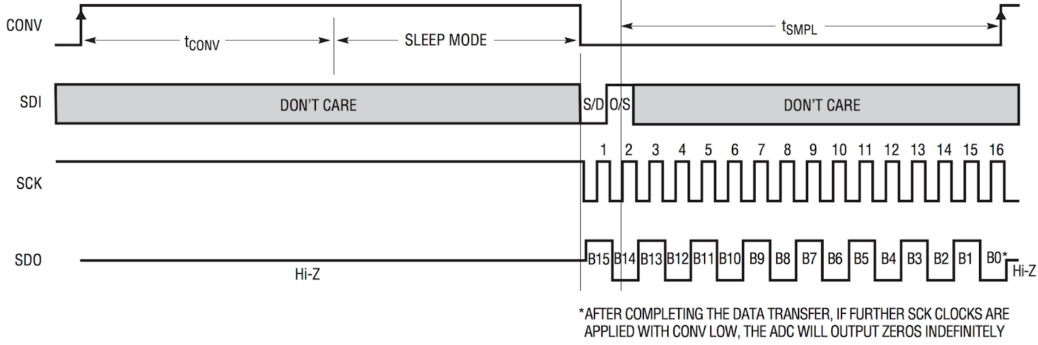


Figure 3.15: LTC1865 Operating Sequence [33]

3.5.4 ROS Architecture

Figure 3.16 shows the ROS architecture of the developed system. In the python script we create a *force_feedback* node. The node is subscribed to X, Y, Z ADC data acquired form sensors and position of the sterile adapter from the daVinci controller. These data are used to find forces. The calculated forces ($force_x$, $force_y$, $force_z$) are then published.

The program calculates magnitude of the forces in X, Y, Z directions using the calibration equation:

$$F = \frac{adc_{data} - b}{a} \quad (3.6)$$

where b is the constant equal to ADC reading when $F = 0$, adc_{data} is current

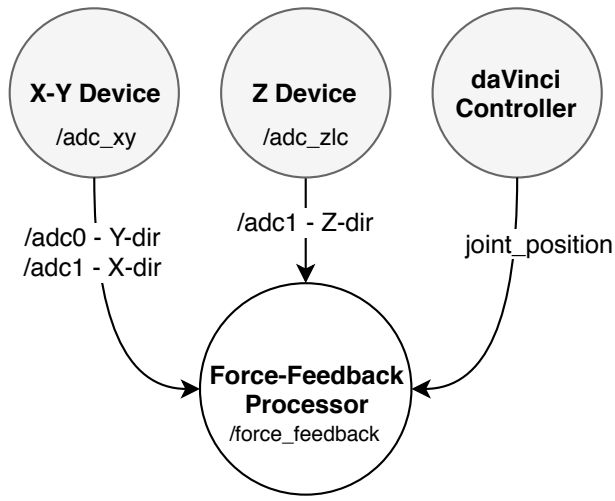


Figure 3.16: ROS Architecture

sensor reading in corresponding direction, and a is linear function of sterile adapter position:

$$a = c \cdot position + d \quad (3.7)$$

where c and d are constants found during calibration and $position$ is the position of the sterile adapter.

Z-device readings does not depend on the position of the sterile adapter. Hence, a has a constant value for Z-device.

3.6 Calibration

3.6.1 Calibration Setup

In order to find parameters of the calibration equation (3.6), the calibration system was developed (Figure 3.17). The load cell and Polaris optical tracking system are used to find "actual" force applied to the tool end. The load cell is used to find the magnitude of the applied force and the optical markers (4-5) to find the direction of the force.

The calibration of the device starts with calibration of the load cell. The daVinci tool is inserted in the sterile adapter. The force readings depend on the position of the sterile adapter, meaning that the force/sensor readings curve should be found for different positions of the adapter. Finding the curve for only two positions would be enough, because the correlation between the curve and position is linear, as the equation (3.7) shows.

Before starting a data collection, the PSM joint of the sterile adapter is fixed in the position 1. After fixing the adapter, in order to transform Polaris camera frame to the robot frame, the transformation matrix should be found. For this purpose, three optical markers (1-3) are attached to the PSM. Z-direction vector corresponds to the vector formed by optical markers (2-1), Y-direction vector is formed by optical markers (2-3). X-direction vector can be found as a cross product between these two

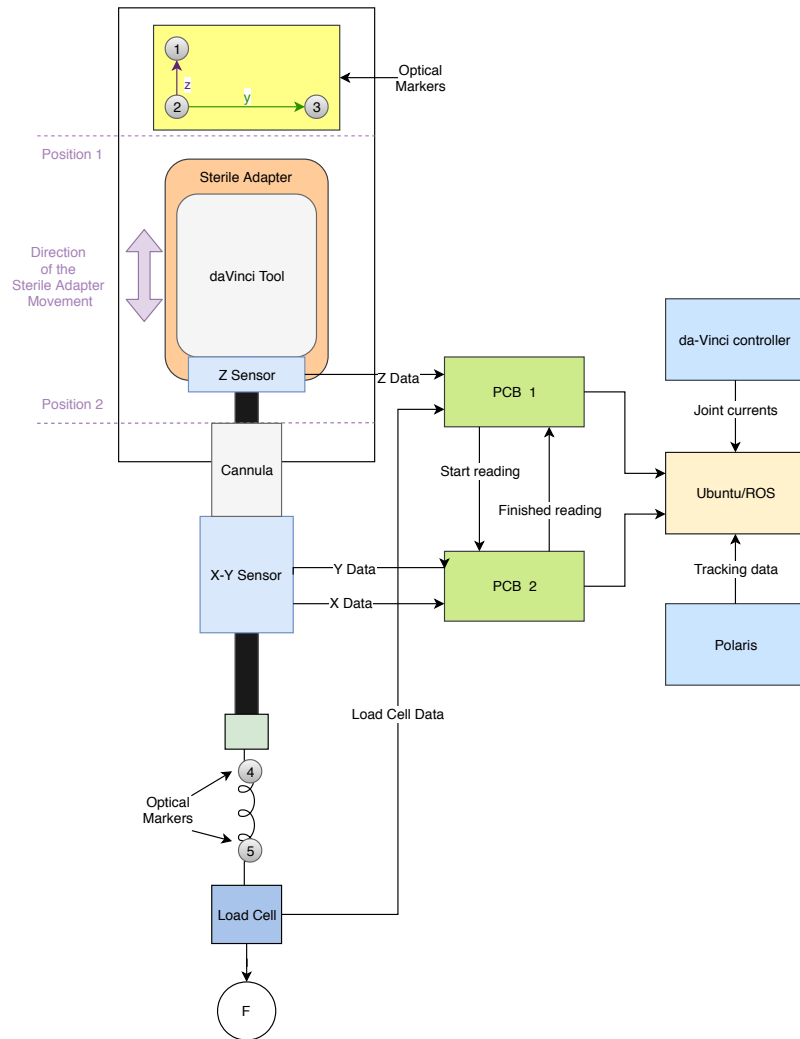


Figure 3.17: Block Diagram of the Calibration Setup

vectors:

$$\vec{X} = \vec{Y} \times \vec{Z} \quad (3.8)$$

The transformation matrix T_c^r is found using coordinates of the \vec{X} , \vec{Y} , \vec{Z} vectors

and coordinates of the optical marker (2) defined as an origin vector.

$$T_c^r = \begin{bmatrix} X_x & Y_x & Z_x & x_0 \\ X_y & Y_y & Z_y & y_0 \\ X_z & Y_z & Z_z & z_0 \\ 0 & 0 & 0 & 1 \end{bmatrix} \quad (3.9)$$

After finding the transformation matrix, the data collection starts. Polaris publishes coordinates of the optical markers (4-5). These coordinates are transformed to the robot frame:

$$P_r = T_c^{r-1} \cdot P_c \quad (3.10)$$

where P_r - coordinates of the marker in the robot frame, P_c - coordinates in the camera frame.

The unit vector of the applied force is found in the robot frame:

$$\vec{U} = \frac{P_5 - P_4}{|P_5 - P_4|} \quad (3.11)$$

where P_5 is the position of the optical marker (5), P_4 is the position of the marker (4), they both are in the robot frame.

The vector of the applied force in the robot frame can be found:

$$\vec{F} = F_m \cdot \vec{U} \quad (3.12)$$

where F_m is the force magnitude found using the load cell. At the same time data from X, Y, Z sensors is collected. The collected data is used to find calibration equation parameters.

3.6.2 Calibration of the Load Cell

The calibration of the load cell is a part of the calibration process of the created device. The block diagram of the setup for the load cell calibration is shown in Figure 3.18. The force F was applied on the load cell using weights, its value:

$$F = mg \quad (3.13)$$

where m is mass of the weight and g is the gravitational constant.

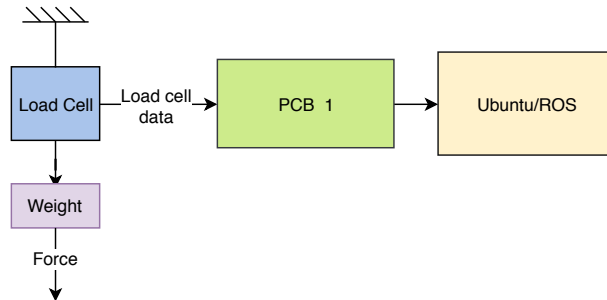


Figure 3.18: Block Diagram of the Load Cell Calibration Setup

The calibration equation for the load cell is following:

$$F_m = adc_{lc} * a_{lc} + b_{lc} \quad (3.14)$$

where adc_{lc} is acquired ADC data from the load cell; a_{lc} and b_{lc} are constants of the linear equation.

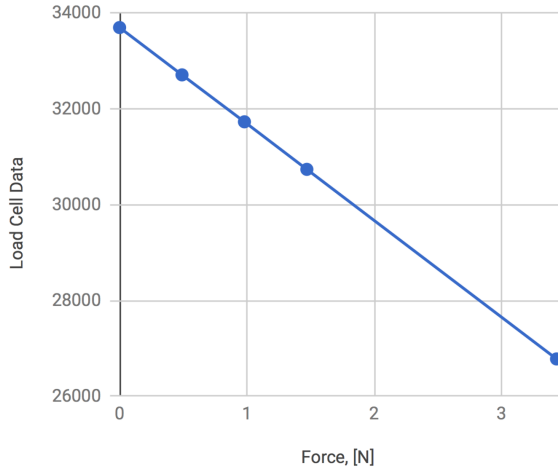


Figure 3.19: Load Cell Calibration Result

Calibration resulted in parameters of the linear equation being $a_{lc} = -4.95 \cdot 10^{-4}$ and $b_{lc} = 16.6$. These values were used to find the magnitude of the applied force on the tool end during X-Y and Z devices calibration.

3.7 Results

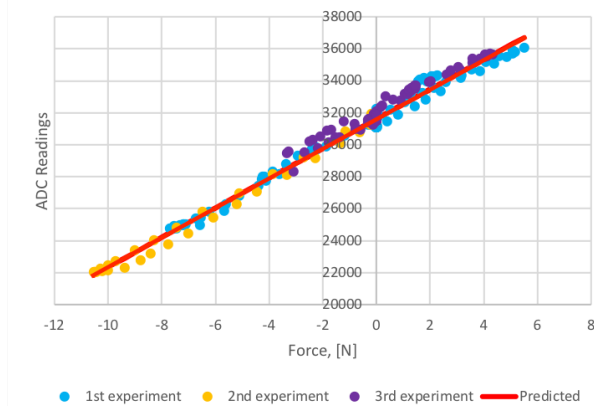
3.7.1 Calibration Results

The calibration results are shown on Figures 3.20 - 3.21, where blue dots are sensor readings and the calibration function shown as a red line. The results for the Z device are presented on Figure 3.21(a). As an alternative method to evaluate forces exerted in a Z-direction we used joint effort readings (Figure 3.21(b)). This method is simple

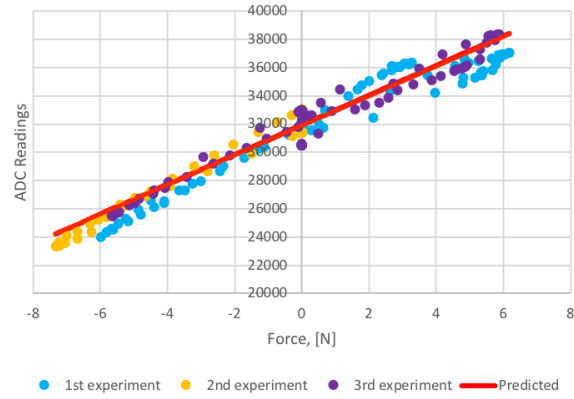
to implement by subscribing to the joint efforts of the daVinci controller and can be used for comparison with created Z-device.

The performance of the created devices was evaluated using standard sensor characteristics, such as absolute error, signal to noise ratio, root mean square error, sensitivity, hysteresis, and measurement range.

All the following information about sensor characteristics is from [34].



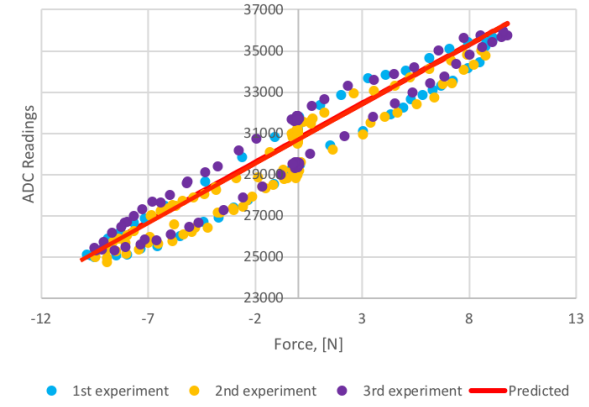
(a) X-direction



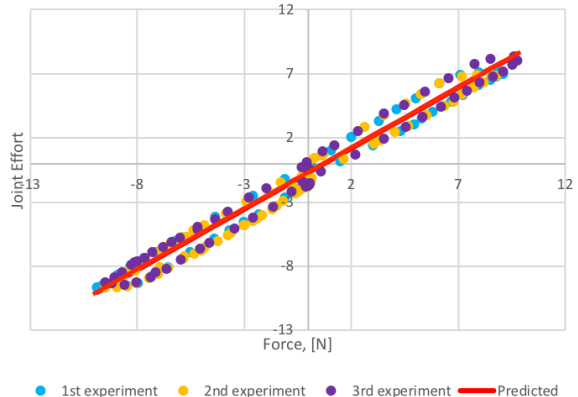
(b) Y-direction

Figure 3.20: Calibration Results of XY Device (n=3)

The accuracy of the developed sensory systems was assessed using the Root Mean



(a) Z Device



(b) Joint Effort

Figure 3.21: Calibration Results in Z-direction (n=3)

Square Error (RMSE), which is:

$$RMSE = \sqrt{\frac{\sum_{i=1}^n (\hat{y}_i - y_i)^2}{n}} \quad (3.15)$$

where \hat{y}_i is predicted with equation (3.6) force value ; y_i is observed "actual" force value found using load cell and Polaris; n is number of observations. RMSE values of all systems are high, meaning low accuracy of the developed system.

The error is the difference between the actual value of the force and the value produced by the system (Equation 3.16). Errors are related to accuracy and can be caused by different sources. In our case all errors were higher than 0.05 N, meaning that system does not meet accuracy requirements.

$$error = \hat{y}_i - y_i \quad (3.16)$$

One of the measurements of signal quality is signal-to-noise ratio (SNR). A higher value of SNR means the clear acquisitions with low signal distortions and artifacts caused by unwanted noise. It is defined as:

$$SNR = \frac{\mu}{\sigma} \quad (3.17)$$

where μ is the mean value of the signal, σ is the standard deviation of the noise. SNR values for all systems are bigger than 1, meaning that all systems have relatively low noise.

The slope of the calibration curve is used for the sensitivity S calculation.

$$S = Dy/Dx \quad (3.18)$$

where Dy is the incremental change in the sensors output, Dx is the incremental change of the force. All the systems have relatively high sensitivity.

Resolution is the smallest change of the applied force that gives a noticeable change

in the sensor output, it is limited by the signal noise. Devices have higher resolution than required 0.3 N.

The linearity of the system is the proximity of the calibration curve to the straight line. R^2 is used to evaluate linearity by measuring the closeness of the measured data to the fitted regression line. Generally, strain gauges have the linear response with deformation and all sensors showed high linearity with R^2 higher than 90%.

Hysteresis is the difference between sensor outputs when the sensor is loaded versus unloaded. All sensors have shown high hysteresis, up to 2.8 N.

The measurement range consists of the maximum and minimum values of the force that can be measured with created systems. For the created system, it corresponds to force values, when the output signal reaches saturation. However, for Z-directional measurements, when z-component of the applied force was higher than 12 N it caused sliding of the sterile adapter. Meaning physical limitation for Z-direction force measurements. All designed devices measure forces in slightly higher than $\pm 11N$ range. When the applied force exceeds the specified range, the device readings can be used to trigger safety alert.

Precision represents the ability of the system to give the same output under the same conditions. The precision of the system was assessed by the standard deviation of the sensor outputs when similar forces were applied. All sensors have low precision, which is reflected in high absolute errors values.

All sensor characteristics were calculated for X-Y device, Z-device, and Z-direction

evaluation joint effort method and provided in the Table 3.3. For each sensor, the calculated sensor characteristics are average values from the results of 3 trials.

Table 3.3: Sensors Characteristics

	X-sensor	Y-sensor	Z-sensor	Joint Effort
Error \pm SD, N	0.059 ± 0.435	0.017 ± 0.755	-0.716 ± 1.324	-1.411 ± 0.672
RMSE	0.44	0.75	1.5	1.56
S/N	2888	3041	114	566
Noise SD, N	0.011	0.004	0.115	0.017
Sensitivity	911	1030	618	0.977
Precision, N	0.4	0.65	0.63	0.35
Resolution, N	0.03	0.02	0.2	0.03
R^2	0.965	0.924	0.938	0.963
Range, N	-19 to 23	-18 to 20	-12 to 12	-12 to 12
Hysteresis, N	0.99	2.4	2.8	1.2

3.7.2 Calibration Curve Dependence from Sterile Adapter Position

Movement of the sterile adapter joint causes change of the moment arm length (L_{gauge} on Figure 3.22).

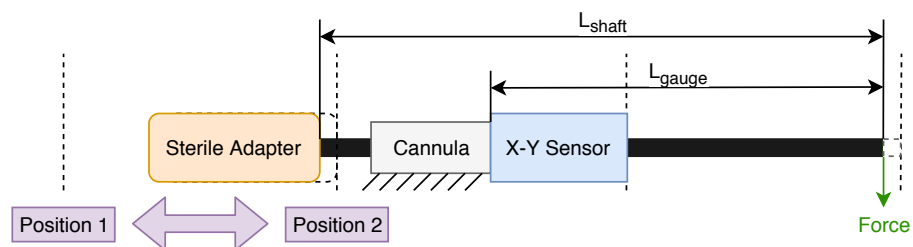


Figure 3.22: Sterile Adapter Movement

The force applied on the X-Y sensor F_{sensor} linearly depends on the moment arm length:

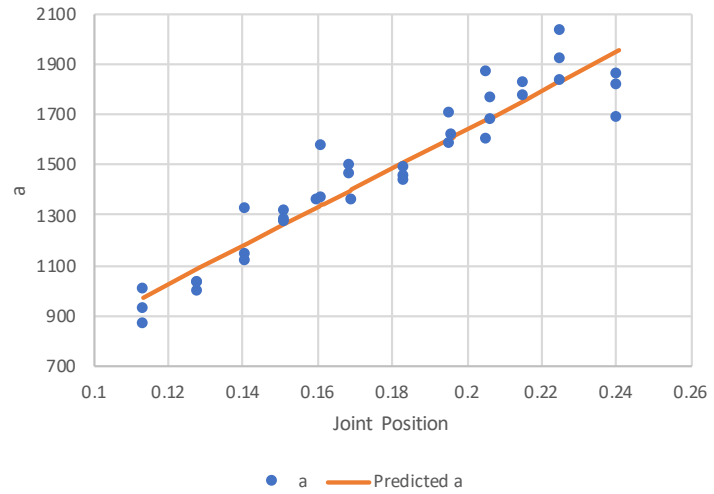
$$F_{sensor} = \frac{L_{shaft}}{L_{gauge}} \cdot F_{tool} \quad (3.19)$$

where F_{tool} is the force applied on the tool end, L_{shaft} is the length of the shaft.

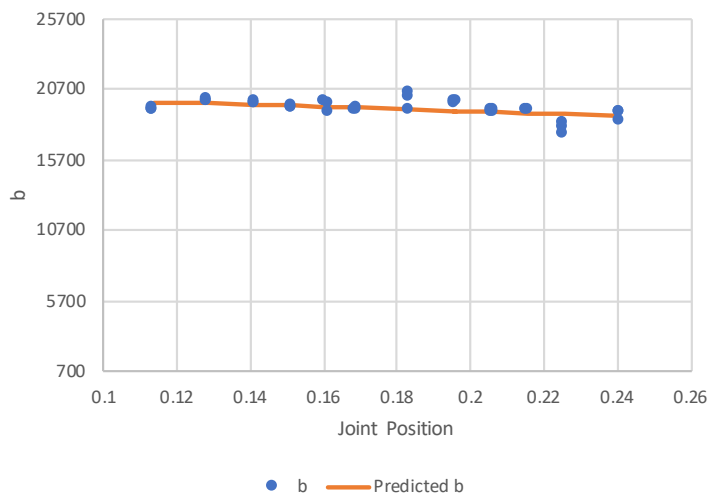
The dependence between position of the sterile adapter and calibration curve constants (a and b from equation 3.6) is linear for X and Y force components (Figures 3.23 - 3.24). We ran 3 trials for each position.

The R^2 of constant a is 0.9 for X-component of the force, 0.827 for Y-component. The low linear fit is caused by considerable systematic errors of the sensors.

Constant b does not depend on the sterile adapter position and changes due to systematic errors and noise in the system.

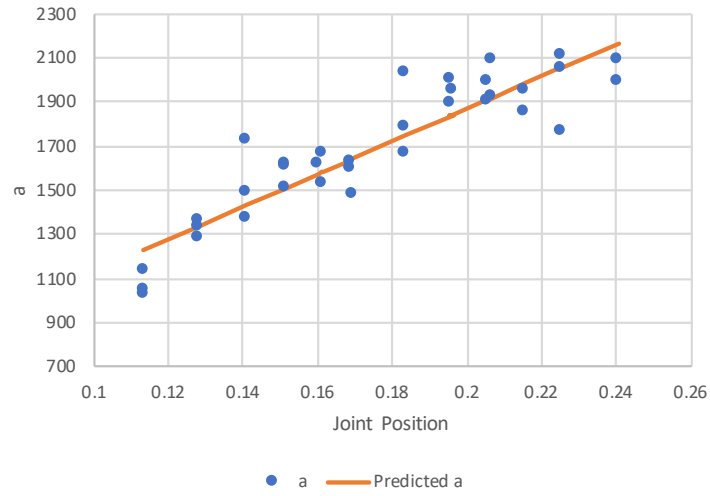


(a) Constant a

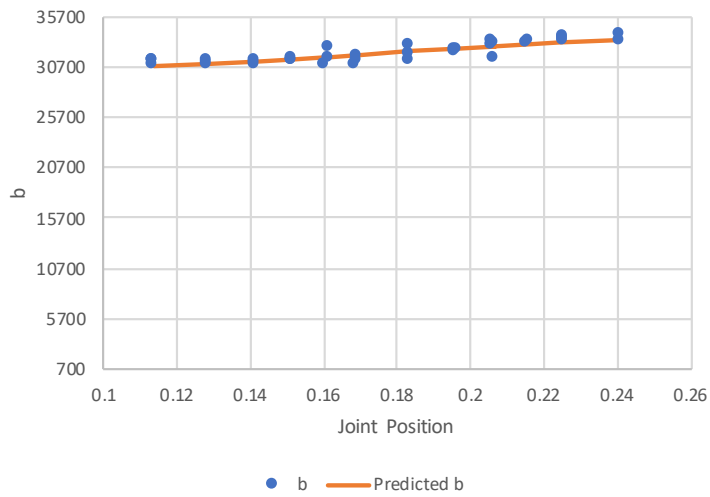


(b) Constant b

Figure 3.23: Sterile Adapter Position Calibration Results for X-direction



(a) Constant a



(b) Constant b

Figure 3.24: Sterile Adapter Position Calibration Results for Y-direction

Chapter 4

Discussion and Conclusion

The results have shown that the developed system is linear and has high sensitivity, appropriate measuring range, high resolution, and low noise. In addition, the results from FFT analysis have shown that the developed PCB gives low noise output. The noise is outside frequency range of the original signal and can be easily filtered out using digital low pass filter.

At the same time, the sensory system has high absolute errors, high RMSE, low precision, and significant hysteresis. Figure 4.1 shows X-component of the force measured at the same time using the X-Y device and using "actual force" data from the load cell. The error value changes simultaneously with rapid changes of the force applied. Taking into account, the low noisiness of the system, plausible explanation of the fluctuations in the output signal is systematic errors. Important to note, that the errors could be related to the high hysteresis of the sensors.

4.1 Mechanical Design Issues

The force-sensing devices were designed so they can easily fit the daVinci cannula and the sterile adapter. The tolerances are compensated by adjustment of the set screws, giving good modularity of the system.

One of the disadvantages is the addition of the weight to the arm, that can alter robot performance. Taking into account, that the device will be placed close to the center of rotation of the robot arm, it will have minimal effect on the moment of inertia in comparison to sensors added to the grippers.

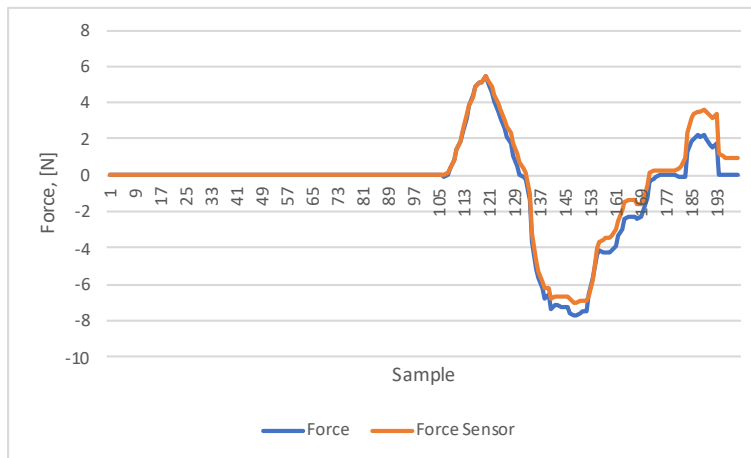


Figure 4.1: Actual and Measured Forces in X-direction

The calibration curve for Y-directional sensor has higher absolute error values, higher RMSE and lower linearity in comparison to X-directional sensor. The reason for that could be mechanical design issues caused by manufacturing problems (Figure 4.2). Different thicknesses of the walls, where sensors applied, cause different strain values for positive and negative directions of the force.

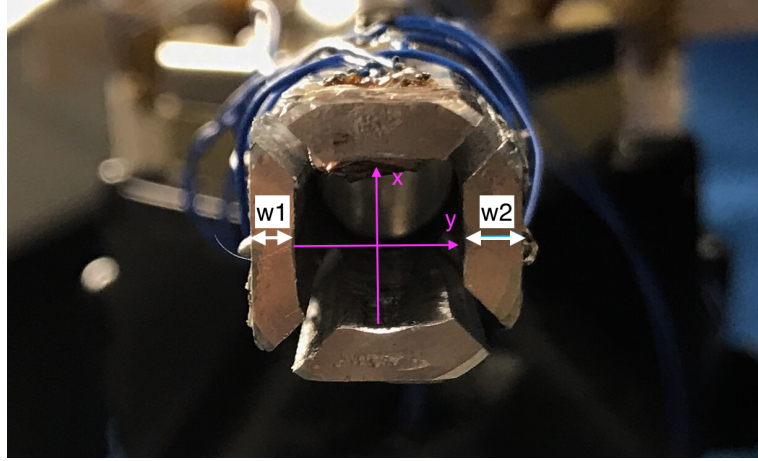


Figure 4.2: Lower Face of the X-Y Device without Tool Shaft

Comparison of two Z-component of the force measurement methods has shown, that Z Device has lower signal-to-noise ratio, lower resolution, lower linearity, and higher hysteresis. Even though the joint effort method is slightly better than the created device, it does not comply with all sensor requirements, and it is hard to change the output results for this method. The major advantage of the created Z Device is the ability to improve it. For example, hysteresis can be reduced by changing the force measurement plate material and its thickness.

The system has separate Wheatstone bridges for each direction, giving the ability to measure each component of the force independently. However, Z Device and the X-Y device cannot work together at the same time, because created X-Y device takes the Z-component of the force and slightly restricts rotation of the shaft. In order to solve that issue, we can change the mechanical design of the X-Y device by increasing the size of the sleeve and adding slippery material between the shaft and the sleeve (Figure 4.3). However, it will cause other issues with increased incision size to 1.9

cm. It is still in the appropriate range (1-2 cm) [35], however, the patient recovery time would increase. Another option could be moving the X-Y device on the top of the cannula or changing the cannula design and applying sensors on it.

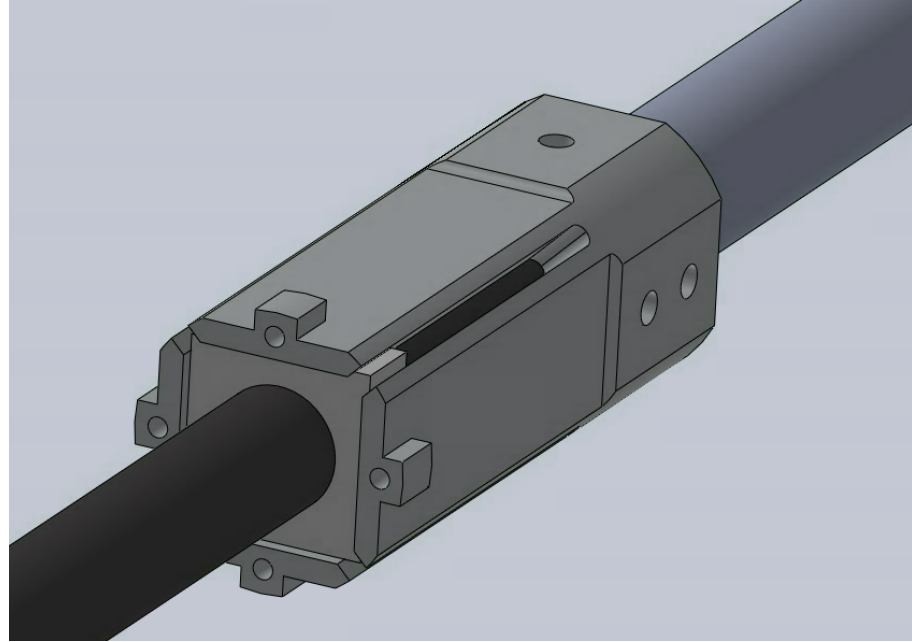


Figure 4.3: New X-Y Device Design

Both devices should undergo sterilization. XY device goes inside the patient, meaning that it should be created using biocompatible materials. The current version of the device is not biocompatible. The biocompatibility can be achieved using stainless steel as a device material and biocompatible epoxy to cover strain gauges, also Teflon coated wires should be used for all electrical connections. Use of stainless steel will require the change of the device dimensions since the material has different elasticity.

4.2 Electrical Design Issues

The real-time haptic feedback requires minimum data acquisition speed to be 1 kHz [25]. However, the current maximum speed is 588 Hz due to the limitation of data transfer speed of serial communication (115.2 Kbps). In order to increase the speed, the communication channel can be changed to SPI (up to 10 Mbps) [36] or one of the wireless protocols, such as Bluetooth (up to 1 Mbps) or wifi (up to 100 Mbps) [37]. Also, the communication protocol between microcontroller and ADC can be changed from SPI to faster parallel communication. Additionally, the microcontroller can be changed to faster one, so it can support wireless communication. All these changes require the change of the PCB design and microcontroller software.

Also, in the PCB the amount of Wheatstone bridges and ADCs should be increased from 2 to 4 to reduce the overall size of the system by removing second PCB and master-slave communication.

4.3 Conclusion

The created sensor gives 3-DOF force feedback by using lateral force sensing in a compact modular approach, the novel axial force sensing approach, and a custom ros-enabled sensor interface. New calibration approach of the force sensing devices was created. The contributions show that it is possible to add force-feedback in the daVinci robot without major changes of the existing system. However, not all of the

requirements for the force measuring system were satisfied, meaning that the sensors need further improvements in both electrical and mechanical designs.

References

- [1] Intuitive surgical, inc. - da vinci surgical system. [Online]. Available: <https://www.intuitivesurgical.com/>
- [2] A. M. Okamura, “Haptic feedback in robot-assisted minimally invasive surgery,” vol. 19, no. 1, pp. 102–107.
- [3] C. E. Reiley, T. Akinbiyi, D. Burschka, D. C. Chang, A. M. Okamura, and D. D. Yuh, “Effects of visual force feedback on robot-assisted surgical task performance,” vol. 135, no. 1, pp. 196–202.
- [4] O. A. J. van der Meijden and M. P. Schijven, “The value of haptic feedback in conventional and robot-assisted minimal invasive surgery and virtual reality training: a current review,” vol. 23, no. 6, pp. 1180–1190.
- [5] M. Tavakoli, *Haptics for Teleoperated Surgical Robotic Systems*. World Scientific, google-Books-ID: 9UNkDQAAQBAJ.
- [6] A. R. Lanfranco, A. E. Castellanos, J. P. Desai, and W. C. Meyers, “Robotic surgery,” vol. 239, no. 1, pp. 14–21.
- [7] B. S. Peters, P. R. Armijo, C. Krause, S. A. Choudhury, and D. Oleynikov, “Review of emerging surgical robotic technology,” vol. 32, no. 4, pp. 1636–1655.
- [8] S.-C. Lim, H.-K. Lee, and J. Park, “Role of combined tactile and kinesthetic feedback in minimally invasive surgery,” vol. 11, no. 3, pp. 360–374.
- [9] C. C. J. Alleblas, M. P. H. Vleugels, S. F. P. J. Coppus, and T. E. Nieboer, “The effects of laparoscopic graspers with enhanced haptic feedback on applied forces: a randomized comparison with conventional graspers,” vol. 31, no. 12, pp. 5411–5417.

- [10] M. E. Currie, A. Talasaz, R. Rayman, M. W. A. Chu, B. Kiaii, T. Peters, A. L. Trejos, and R. Patel, “The role of visual and direct force feedback in roboticsassisted mitral valve annuloplasty,” vol. 13, no. 3.
- [11] M. B. Hong and Y. H. Jo, “Design and evaluation of 2-DOF compliant forceps with force-sensing capability for minimally invasive robot surgery,” vol. 28, no. 4, pp. 932–941.
- [12] C. Ho, E. Tsakonas, K. Tran, K. Cimon, M. Severn, M. Mierzwienski-Urban, J. Corcos, and S. Pautler, *HEALTH SERVICES IMPACT*. Canadian Agency for Drugs and Technologies in Health. [Online]. Available: <https://www.ncbi.nlm.nih.gov/books/NBK168924/>
- [13] H. Su, I. I. Iordachita, J. Tokuda, N. Hata, X. Liu, R. Seifabadi, S. Xu, B. Wood, and G. S. Fischer, “Fiber-optic force sensors for MRI-guided interventions and rehabilitation: A review,” vol. 17, no. 7, pp. 1952–1963.
- [14] J. Peirs, J. Clijnen, D. Reynaerts, H. V. Brussel, P. Herijgers, B. Corteville, and S. Boone, “A micro optical force sensor for force feedback during minimally invasive robotic surgery,” *Sensors and Actuators A: Physical*, vol. 115, no. 2, pp. 447 – 455, 2004, the 17th European Conference on Solid-State Transducers.
- [15] W. Schwalb, B. Shirinzadeh, and J. Smith, “A forcesensing surgical tool with a proximally located force/torque sensor,” *The International Journal of Medical Robotics and Computer Assisted Surgery*, vol. 13, no. 1, p. e1737.
- [16] A. I. Aviles, S. M. Alsaleh, J. K. Hahn, and A. Casals, “Towards retrieving force feedback in robotic-assisted surgery: A supervised neuro-recurrent-vision approach,” vol. 10, no. 3, pp. 431–443.
- [17] Sang Hongqiang, Yun Jintian, Monfaredi Reza, Wilson Emmanuel, Fooladi Hadi, and Cleary Kevin, “External force estimation and implementation in robotically assisted minimally invasive surgery,” vol. 13, no. 2, p. e1824.
- [18] S. M. Yoon, W. J. Kim, and M. C. Lee, “Design of bilateral control for force feedback in surgical robot,” vol. 13, no. 4, pp. 916–925.

- [19] HBM. (2017) Piezoelectric or Strain Gauge Based Force Transducers? [Online]. Available: <https://www.hbm.com/en/3719/piezoelectric-or-strain-gauge-based-force-transducers/>
- [20] A. sensors. (2017) Piezoelectric Sensors and Strain Gauge-based Force Transducers: Principles in Force Measurement. [Online]. Available: <http://www.azosensors.com/article.aspx?ArticleID=281>
- [21] N. I. L. Azaman, M. A. Ayub, and A. A. Ahmad, “Characteristic and sensitivity of quantum tunneling composite (QTC) material for tactile device applications,” in *2016 7th IEEE Control and System Graduate Research Colloquium (ICSGRC)*, pp. 7–11.
- [22] “Quantum tunnelling composites: Characterisation and modelling to promote their applications as sensors,” vol. 164, no. 1, pp. 46–57.
- [23] I. Mack, S. Ferguson, K. Rafferty, S. Potts, and A. Dick, “Interactive force-sensing feedback system for remote robotic laparoscopic surgery,” vol. 34, no. 4, pp. 376–387.
- [24] S. K. Prasad, M. Kitagawa, G. S. Fischer, J. Zand, M. A. Talamini, R. H. Taylor, and A. M. Okamura, “A modular 2-DOF force-sensing instrument for laparoscopic surgery,” in *Medical Image Computing and Computer-Assisted Intervention - MICCAI 2003*, ser. Lecture Notes in Computer Science. Springer, Berlin, Heidelberg, pp. 279–286. [Online]. Available: https://link.springer.com/chapter/10.1007/978-3-540-39899-8_35
- [25] Seungmoon Choi and H. Tan, “Effect of update rate on perceived instability of virtual haptic texture,” vol. 4. IEEE, pp. 3577–3582. [Online]. Available: <http://ieeexplore.ieee.org/document/1389970/>
- [26] ASM material data sheet. [Online]. Available: <http://asm.matweb.com/search/SpecificMaterial.asp?bassnum=ma6061t6>
- [27] MICRO-MEASUREMENTS. (2014) Surface Preparation for Strain Gage Bonding. [Online]. Available: <http://www.vishaypg.com/docs/11129/11129B129.pdf>

- [28] V. P. Group. Cea Strain Gage Installation with M-Bond 200 Adhesive (Training Video) - Micro-Measurements. Youtube. [Online]. Available: <https://www.youtube.com/watch?v=SjXpF61HRys>
- [29] Printed circuit board manufacturer & PCB assembly | advanced circuits. [Online]. Available: <http://www.4pcb.com/>
- [30] F. J. Harris, “On the use of windows for harmonic analysis with the discrete fourier transform,” vol. 66, no. 1, pp. 51–83.
- [31] Filtering and smoothing data - MATLAB & simulink. [Online]. Available: <https://www.mathworks.com/help/curvefit/smoothing-data.html>
- [32] Introduction to arduino SPI library with LTC1286 and DAC714. [Online]. Available: <https://www.allaboutcircuits.com/projects/arduino-spi-library-ltc1286-dac714/>
- [33] “LTC1864/LTC1865 - power, 16-bit, 250ksps 1- and 2-channel ADCs in MSOP,” p. 24.
- [34] K. Kalantar-zadeh, *Sensors Characteristics*. Springer US, pp. 11–28. [Online]. Available: http://link.springer.com/10.1007/978-1-4614-5052-8_2
- [35] Laparoscopy and laparoscopic surgery. surgery information. [Online]. Available: <https://patient.info/health/laparoscopy-and-laparoscopic-surgery>
- [36] UART vs SPI vs i2c | difference between UART,SPI and i2c. [Online]. Available: <http://www.rfwireless-world.com/Terminology/UART-vs-SPI-vs-I2C.html>
- [37] Wireless protocols - WiFi, bluetooth, BT, BTLE, GPS, GPRS, 6lowpan, zigbee, Rowebots bluetooth stack - Rowebots. [Online]. Available: <http://rowebots.com/en/products/unison-rtos-article/wireless-protocols>

Chapter 5

Appendices

Appendix A. Circuit

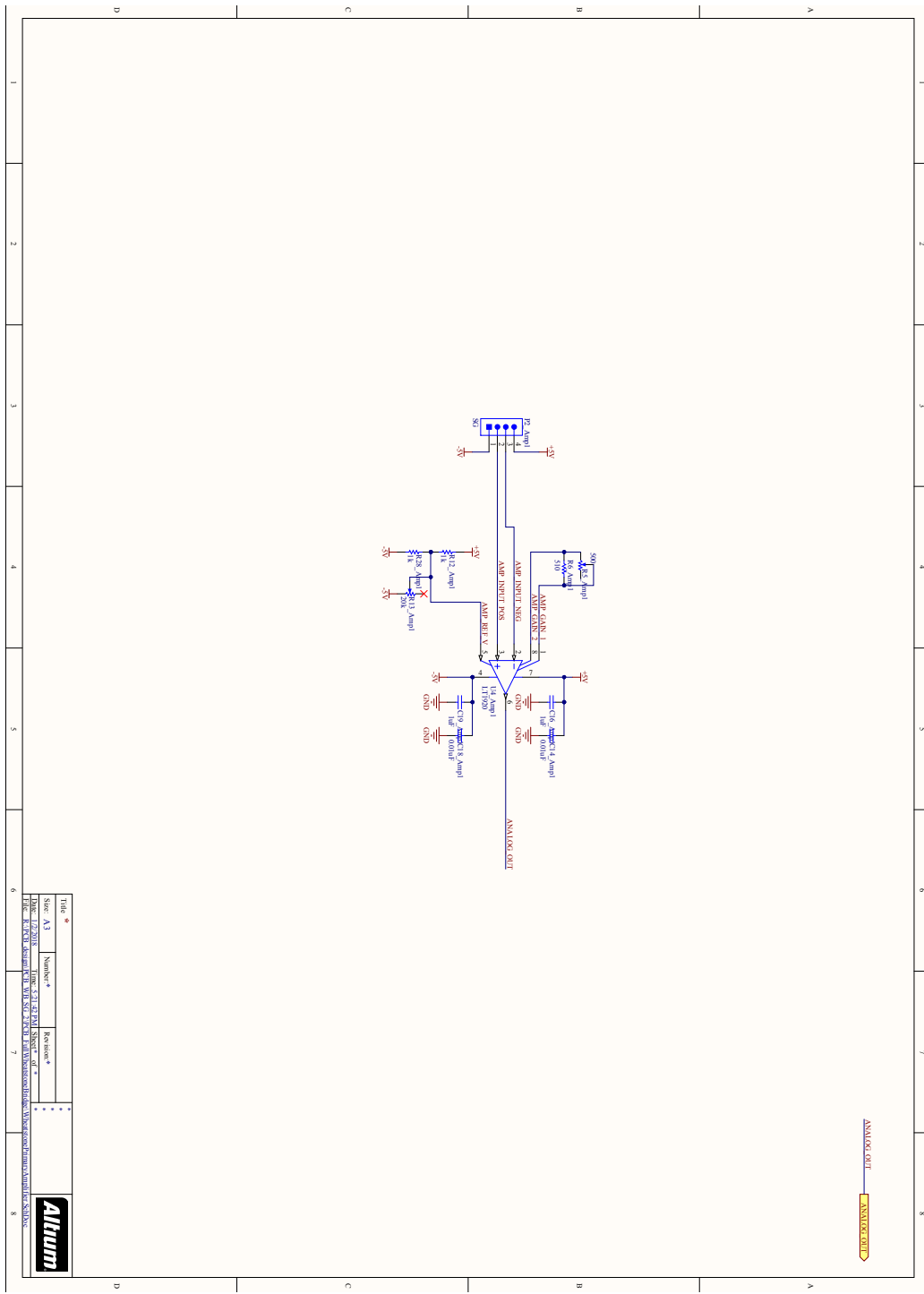


Figure 5.1: 1st Instrumentation Amplifier

Appendix A. *Circuit*

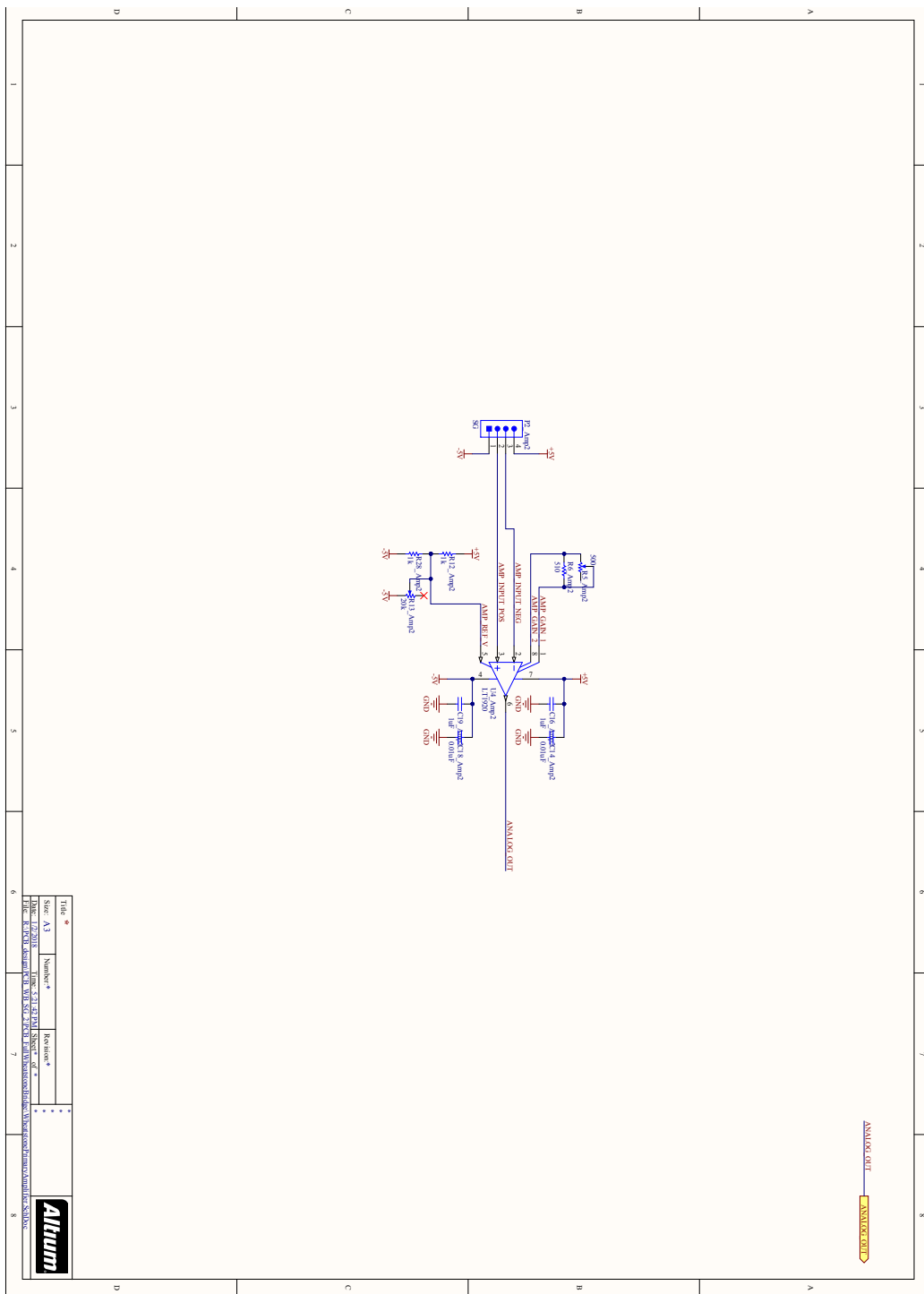


Figure 5.2: 2nd Instrumentation Amplifier

Appendix A. *Circuit*

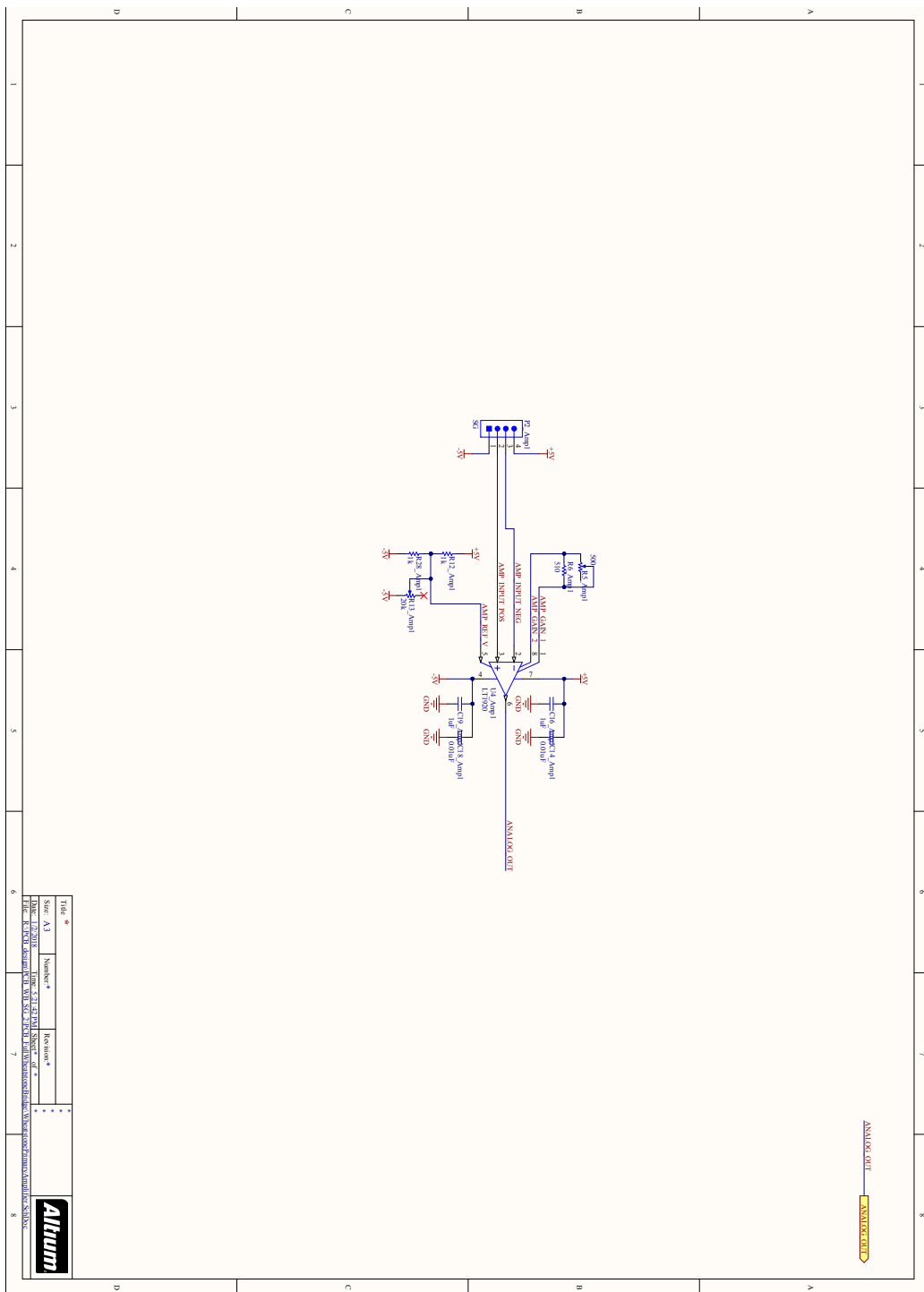


Figure 5.3: USB-UART Interface

Appendix A. *Circuit*

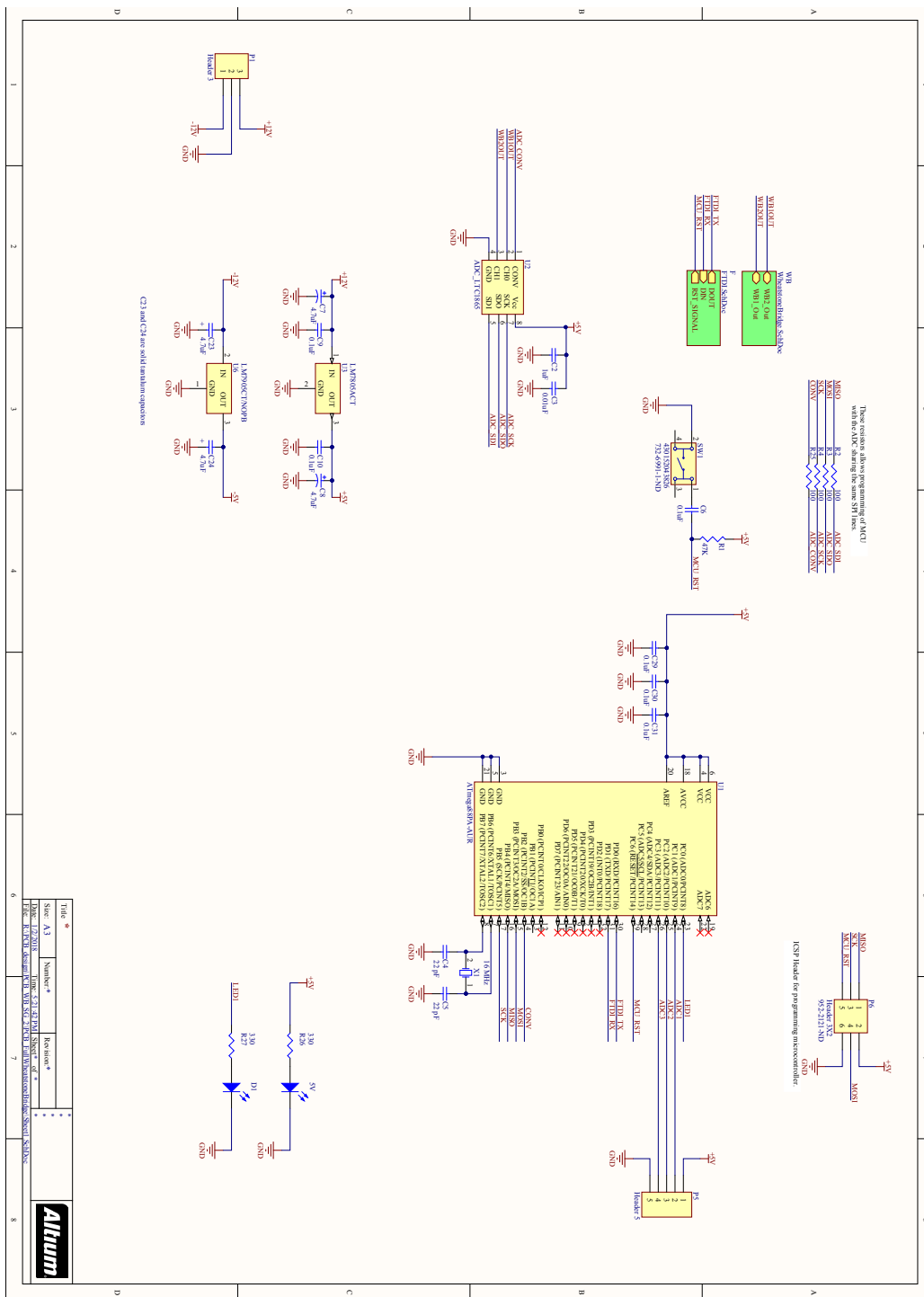


Figure 5.4: Microcontroller and Power Source

Appendix A. *Circuit*

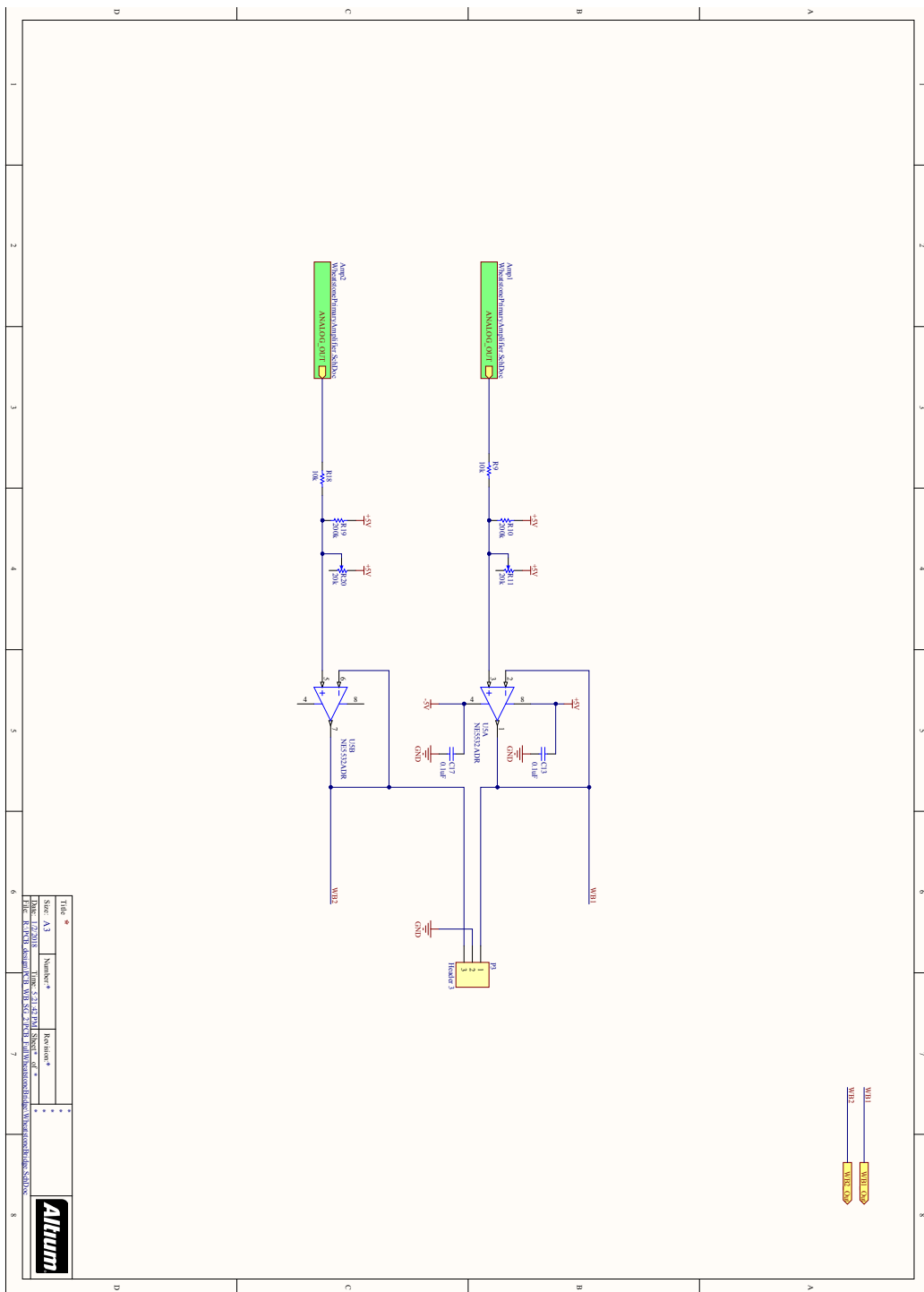


Figure 5.5: Voltage Converter

Appendix A. Circuit

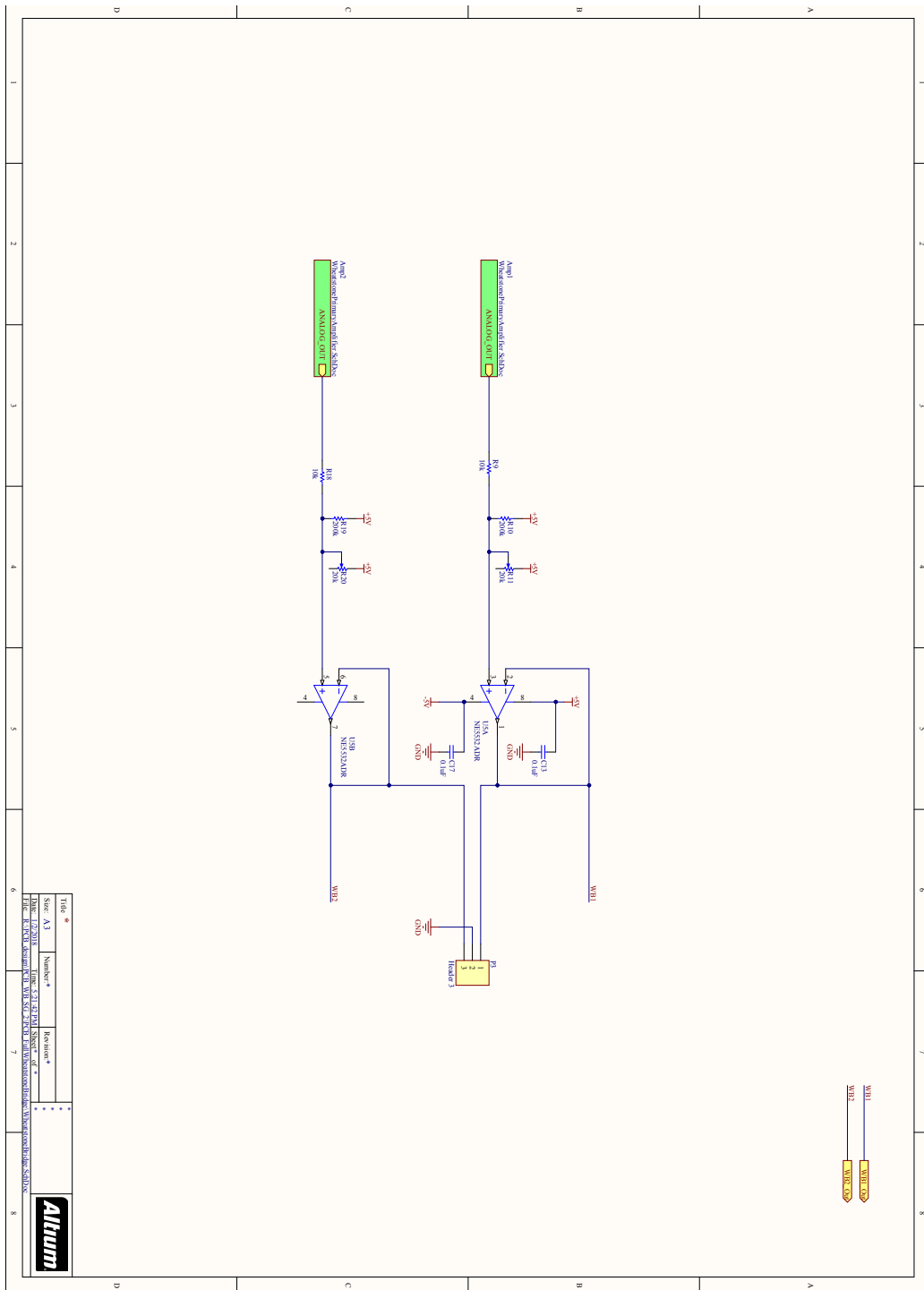


Figure 5.6: PCB Layout